DUAL SCALE POROSITY EFFECTS ON CRACK-DEFECT INTERACTIONS IN ADDITIVELY MANUFACTURED TI-6AL-4V

BY

RAYMUNDO MURO-BARRIOS

THESIS

Submitted in partial fulfillment of the requirements
for the degree of Master of Science in Aerospace Engineering
in the Graduate College of the
University of Illinois Urbana-Champaign, 2021

Urbana, Illinois

Advisers:

Professor John Lambros
Associate Professor Huck Beng Chew

ABSTRACT

Microstructural defects and unpredictable fracture behavior have limited the widespread use of additively manufactured (AM) alloys in load bearing components. In addition to background pores (2-12 μm) nucleated from particle inclusions responsible for ductile fracture in conventional metals, larger defects (20-50 μm) can be introduced during the additive manufacturing process resulting in a dual-scale porosity failure process in AM alloys. The effect of these AM defects on the fracture behavior of AM Direct Metal Laser Melted Ti-6Al-4V has been previously observed in Scanning Electron Microscopy and Digital Image Correlation analyses, which suggest AM defects lead to the premature failure in fracture and fatigue of AM metals. However, the specific failure mechanisms associated with the AM defects have not been identified.

In this thesis, a numerical approach is undertaken to quantitatively elucidate the role of the dual-scale porosity and resulting crack-defect interactions in AM Ti-6Al-4V alloys. A small-scale yielding, modified boundary layer model with imposed monotonically increasing K_I (Stress Intensity Factor) remote displacement loading was used to study crack propagation through a local distribution of dual size-scale voids. The Gurson yield function was implemented to model the background porosity while the larger AM defects were explicitly represented. Micrographs were taken of physical AM Ti-6Al-4V specimen cross-sections to determine the expected size and frequency of AM defects. Fracture resistance curves were generated for random AM void distributions with increasing levels of AM defects. Over and underperforming material samples with off-nominal fracture resistance were analyzed in more detail through observation of 3D void interactions in cross-sectional model images. It is shown that AM defects activate isolated and clustered damage zones ahead of the crack tip, blunt the crack tip, promote crack tortuosity, and at times appear to increase the local material toughness over a conventional alloy. Conversely, planar clusters of AM defects can form preferential crack planes that may be responsible for the premature failure of AM components. Inclusion of the AM defects also generates more opportunities for localized dissipation of plastic work, which suggests the potential for achieving “fracture-by-design” through strategic void placements. Preliminary materials design concepts resulting in significantly improved apparent fracture toughness over conventional alloys are discussed.

ACKNOWLEDGMENTS

First and foremost, I would like to extend my sincere thanks to my advisers, Professor John Lambros and Professor Huck Beng Chew, for their guidance, mentorship, and flexibility throughout every stage of my research and graduate studies. Thank you to the other members of the Lambros and Chew lab groups: Renato, Dev, Yiguang, Sam, Franco, Soumendu, Yue, Michael, Huy, and Ning, for their company, camaraderie through difficult courses, and assistance in both overcoming the learning curve and resolving technical issues throughout my thesis research. I would also like to express my gratitude and appreciation to my loved ones, friends, and broader support network for their help and encouragement throughout this endeavor. Finally, I would like to thank the funding that made this work possible. This work was supported through Stillwell and Master's fellowships from the Department of Aerospace Engineering and the Graduate College at the University of Illinois in Urbana-Champaign and through grant NSF-CMMI-2009684 from the National Science Foundation (NSF) Civil, Mechanical and Manufacturing Innovation (CMMI) and Mechanics of Materials and Structures (MOMS) programs.

TABLE OF CONTENTS

CHAPTER 1 – INTRODUCTION

1.1. Additively Manufactured (AM) Ti-6Al-4V

The emergence of additive manufacturing has provided the aerospace industry freedom to pursue increasingly complex designs typically untenable or unprofitable through traditional manufacturing methods. Several major aerospace companies have already begun implementing additive manufacturing technology into the production of metallic components, such as in Boeing's 787 Dreamliner, the fuel nozzle tips in GE Aviation's LEAP engines, and SpaceX's SuperDraco rocket engines (Najmon et al., 2019). The freeform fabrication possible through additive manufacturing provides engineers freedom to design for weight reduction, increased heat exchange, and cost savings by reducing outside contractors and large amounts of material waste (Liu & Shin, 2019). Additive manufacturing can significantly reduce the number of parts in assemblies as seen in NASA's next generation Space Launch System J-2X engine, where 115 parts in a fuel injector were replaced with just 2 AM components (Kumar & Krishnadas Nair, 2017). By shortening lead times and moving production on-site, additive manufacturing can improve supply chains for spare parts through distributed production, such as in overseas operations of the F-18 Super Hornet or through on demand production of AM components in space (Clinton, 2016; Khajavi et al., 2014). Within the aerospace industry, a common choice for the AM build material is the Ti-6Al-4V alloy due its high strength, low density, high fracture toughness, and exceptional corrosion resistance (Liu & Shin, 2019). Despite the benefits of additive manufacturing, additive manufacturing processes are vulnerable to microstructural irregularities such as the formation of porosity (void defects), increased surface roughness, oxygen enrichment, and residual stresses that result in variability behind the mechanical, especially failure, properties of AM Ti-6Al-4V builds (Liu & Shin, 2019). Although such uncertain failure properties of AM builds currently hinders the widespread application of additive manufacturing, the process-structure-property (PSP) linkage is an active area of research aiming to better understand the relationships between additive manufacturing process parameters, microstructures, and the final mechanical properties that will ultimately enable more widespread use of AM metals for critical load bearing applications.

1.1.1. Additive Manufacturing Methods Review

Additive manufacturing methods for metallic components can typically be categorized as either Powder Bed Fusion (PBF) or Directed Energy Deposition (DED), both of which use a laser or electron beam as an energy source. PBF methods involve the uniform spreading of feedstock material over previous build layers using a roller or blade, while DED methods simultaneously melt and supply the feedstock material directly where needed and can use various source materials (powder, wire, etc.) (Dutta & Froes, 2016; Gibson et al., 2015). AM builds used in this thesis and related works (Foehring et al., 2018; VanSickle et al., 2020) were manufactured though a powder bed fusion method, namely Direct Metal Laser Melting (DMLM). The DMLM process deposits a layer of powder particles using a roller onto a build plate within a temperature-controlled build chamber, where a laser follows a Computer Aided Design (CAD) file geometry to fully melt the powder particles and fuse them with the underlying build material (Dutta & Froes, 2016). Process parameters such as the laser scan speed, laser power, laser bead width, hatch spacing (the distance between subsequent laser passes), powder layer thickness, and build chamber temperature can all affect the propensity for defect formation (Casalino et al., 2015).

Void defects (~20-50 μm in diameter) are introduced during the additive manufacturing process via gas entrapment, melt pool instabilities, and incomplete melting of powder particles often referred to as "lack-of-fusion" (LOF) defects (Snow et al., 2020). Gas entrapment occurs when suboptimal laser parameters deposit excessive energy that vaporizes material deep below the current build layer to cause void cavitation; this process often results in spherical void defects also referred to as "keyholing" defects (Panwisawas et al., 2017). Lack-of-fusion defects are typically elongated in nature (~100 μm) and contain multiple un-melted particles (Snow et al., 2020). Proper calibration of the additive manufacturing process parameters is especially important for complex and thin AM builds, which are susceptible to increased AM void defects due to poor heat dissipation at the build surface by the surrounding powder bed (*Get the Facts On… Porosity in Metal Additive Manufacturing | GE Additive*, 2021; Wu et al., 2020).

Components produced via DMLM are known to exhibit unpredictable mechanical properties due to the inclusion of these Additive manufacturing process flaws. Static mechanical properties of PBF AM materials, such as yield strength and ultimate tensile stress, have been found in cases to be equal or greater than their wrought counterparts, but are associated with reduced ductility attributed to fine microstructures that inhibit dislocation motion (Snow et al., 2020). Fatigue life also varies significantly in AM Ti-6Al-4V specimens, even when prepared using identical procedures. Surface roughness plays a significant role in the fatigue life and premature failure is known to be caused in part by the presence of large AM void defects near the specimen surface (Chastand et al., 2018; Snow et al., 2020; VanSickle et al., 2020).

In conventional metals, the nucleation, growth, and eventual coalescence of microvoids resulting in ductile fracture are well established failure processes (Faleskog & Shih, 1997; Stone et al., 1985). Metals that fail through ductile processes typically contain small inclusions that act as nucleation sites for microvoids (2-12 μm) at low stress levels through the brittle cracking or decohesion of particulates (Cui et al., 2020). As these nucleated microvoids grow, locally intense triaxial stress fields induce the formation of new microvoids at neighboring inclusions, which in turn coalesce and form an incipient crack within the material. In addition to these background microvoids, the presence of additional AM defects in AM Ti-6Al-4V introduces a dual-scale porosity in the microstructure: the larger-scale voids (~20-50 μm in diameter) are the AM defects resulting from the additive manufacturing process while the smaller-scale voids (2-12 μm in diameter) are the intrinsic background voids which nucleate from inclusions at low stress levels in conventional alloys. The interactions between these two scales of voids and their effect on the crack path and fracture toughness are still not well established.

1.1.2. Modeling Ductile Fracture of AM Metals

A numerical approach that elucidates the relationships between crack-defect interactions and fracture toughness is needed to better understand the effects of the dual-scale porosity on the failure mechanics of AM Ti-6Al-4V components. A variety of numerical approaches have been proposed to model the micromechanical processes of void growth and coalescence that occur within the fracture process zone (FPZ) of ductile metals. In the past, 2D calculations which model the FPZ of porous materials as a single row of void-containing computational cells based on the well-established constitutive framework for ductile fracture via the Gurson yield function have been used (Chew et al., 2005; Faleskog et al., 1998; Gurson, 1977; Tvergaard, 1989). To simulate the interactions between the dual-scale porosity of the FPZ in AM metals and their influence on the crack path and ductile fracture process, Cui et al. (2020) introduced two size-scales of voids that were randomly seeded throughout a 2D FPZ modeled with several rows of void-containing computational cell elements governed by the Gurson yield function. However, fracture is an inherently 3D phenomenon and perhaps a more representative model is that of Srivastava et al., (2014, 2017), which introduced microvoids of varying sizes within a larger 3D FPZ.

In this thesis, we expand upon the model suggested in Cui et al. (2020) and explore the 2D and 3D modeling of AM defect-crack interactions to calculate the crack growth resistance of AM Ti-6Al-4V specimens. Randomly distributed AM voids are introduced within a pre-defined 2D or 3D FPZ embedded in a modified boundary layer model subjected to remote mode I loading under small-scale yielding conditions. In both the 2D and 3D models, the background porosity is modeled implicitly and in a continuum fashion with computational cells governed by the Gurson yield function, as is typically done for conventional metals, while different densities of AM void defects are modeled explicitly as voids randomly distributed within the FPZ. The effect of T-stress on the fracture response are also briefly explored. Computations of the fracture resistance curves in relation to snapshots of the cross-sectional planes of void growth and material damage within the FPZ provide detailed insights into the common damage dissipation mechanisms associated with crack-defect interactions in AM Ti-6Al-4V.

1.2. Objectives

The goal of this research is to elucidate the relationships between dual-scale porosity and crack-defect interactions in AM Ti-6Al-4V to better predict the fracture response of AM components. Specifically, the objectives are:

(1) Explore the impact of the dual-scale porosity on failure predictions of cracked AM metals. In particular, we would like to explore how each length-scale influences fracture properties such as crack growth resistance curves, and to what extent these influences are coupled between the two length scales.

(2) Identify the role of AM defects in controlling crack path tortuosity, which has been observed experimentally to be more significant in fracture of AM Ti-6Al-4V compared to conventional Ti-6Al-4V.

(3) Understand and quantify the variability of AM metal fracture properties and investigate the way and extent this variability is dependent on the dual-scale porosity.

1.3. Overview

The preceding information in this chapter attempts to cover the fundamental points concerning the variability of failure properties in AM Ti-6Al-4V including a brief review of AM methods, the dual-scale porosity in AM metals, and previous models used to study fracture in ductile metals. Chapter 2 will cover the numerical approach proposed in this study, including details of the modified boundary layer model and the Gurson model, as well as the AM defect representation used in this thesis. Chapter 3 explores the effect of random AM void distributions on the fracture initiation toughness, steady-state fracture toughness, and energy dissipated in both the 2D and 3D models and relates them to damage maps depicting the distribution of damage (void growth) surrounding a crack. Chapter 4 focuses on some of the main deficiencies of the model, discusses crack-defect interactions, and suggests possible future work, including the potential for achieving “fracture-by-design” with strategic AM void placements that can improve the fracture toughness and energy dissipation of AM Ti-6Al-4V over conventional alloys. Lastly, Chapter 5 provides a summary of crack-defect interactions and their effects on the variability of the fracture response in AM Ti-6Al-4V.

CHAPTER 2 – NUMERICAL APPROACH

2.1. Boundary Value Problem

A semi-infinite crack in a modified boundary layer (MBL) model subjected to displacement-controlled, far-field K_I loading under small scale yielding conditions was used to investigate crack-defect interactions in AM Ti-6Al-4V (Fig. 2.1). An elastoplastic material was assumed throughout the model, with Young's modulus E, uniaxial yield strength σ_0, Poisson's ratio ν, and power law strain hardening exponent N. The uniaxial tension stress-strain response is characterized by the true stress-strain relation.

$$\varepsilon = \frac{\sigma}{E}, \sigma < \sigma_0 \tag{2.1}$$

$$\varepsilon = \frac{\sigma_0}{E}\left(\frac{\sigma}{\sigma_0}\right)^{\frac{1}{N}}, \sigma \geq \sigma_0$$

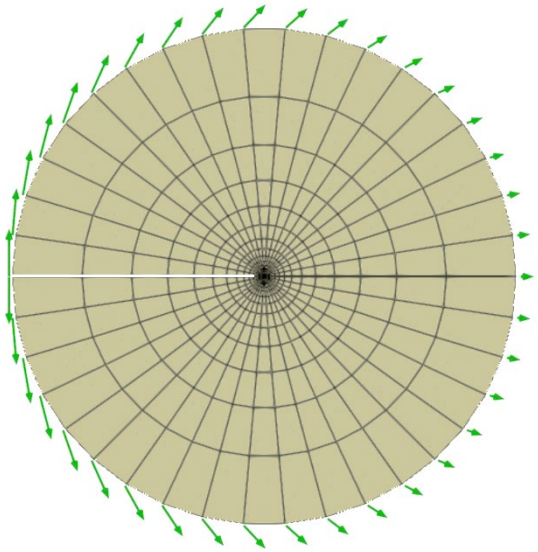

Figure 2.1. *K_I displacement fields prescribed on the MBL model outer boundary*

Finite strains were implemented for all analyses, except for 2D models under plane strain conditions which utilized small-strain assumptions in the solutions to avoid numerical instabilities. The open-source code WARP3D was used for the finite element analyses while Paraview was adopted for simulation

visualization (Ayachit, 2015; Koppenhoefer et al., 1994; *ParaView*, 2021; *WARP3D*, 2021). Because WARP3D is a 3D finite element code, the finite element models for the 2D analyses are comprised of a single plane of 8,865 3D 8-noded brick elements (i.e., unit thickness). Displacements are constrained in the out-of-plane (thickness) direction under 2D plane strain conditions, or with traction-free boundary conditions imposed under 2D plane stress conditions. 3D analyses were carried out using models with a thickness of 10 elements for a total of 88,650 elements; roller boundary conditions were imposed on the nodes of all elements along the inner plane surface, while nodes of all elements along the outer plane surface were traction-free. For nodes along the outer boundary, displacements were monotonically applied following the elastic asymptotic mode I displacement fields

$$u_1(R,\theta) = K_I \frac{1+\nu}{E}\sqrt{\frac{R}{2\pi}}\cos\left(\frac{\theta}{2}\right)\left(\kappa - 1 + 2\sin^2\left(\frac{\theta}{2}\right)\right) \tag{2.2}$$

$$u_2(R,\theta) = K_I \frac{1+\nu}{E}\sqrt{\frac{R}{2\pi}}\sin\left(\frac{\theta}{2}\right)\left(\kappa + 1 - 2\cos^2\left(\frac{\theta}{2}\right)\right)$$

where $R^2 = x^2 + y^2, \theta = \tan^{-1}\left(\frac{y}{x}\right)$ with x and y being Cartesian coordinates centered at the crack notch-tip for nodes on the model boundary, $\kappa = 3 - 4\nu$ under plane strain conditions and $\kappa = \frac{3-\nu}{1+\nu}$ under plane stress conditions. *T*-Stresses, when employed, were imposed as initial residual stresses along the x-direction (σ_{xx}) in the MBL model at the start of the analysis as done in Tvergaard & Hutchinson (1994), Xia (1995), and Xia & Shih, (1996).

Throughout this thesis, the "notch-tip" refers to the initial, undeformed position of the semi-infinite crack-tip. The finite element mesh was refined within a rectangular grid directly ahead of the crack notch-tip to capture the detailed interaction of the propagating crack with AM defects within the fracture process zone (FPZ). The FPZ is comprised of 120 (x) by 53 (y) elements, each of dimensions $D \times D \times D$, where D is the side length of each cubic element in the grid (Fig. 2.2). The remote boundary of the MBL model is

40,000 times the element size D within the process zone, which ensures that small scale yielding conditions are maintained even during crack propagation within the FPZ (typically restricted to half the FPZ length).

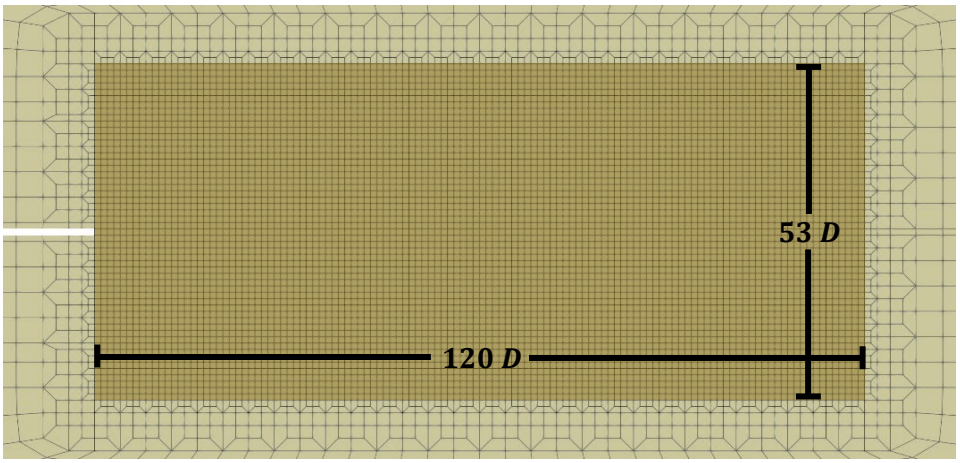

Figure 2.2. *Refined mesh forming the Gurson cell fracture process zone*

2.2. The Gurson Model

There are two different size-scales of voids of concern within the FPZ of AM metals: the background porosity which originates from nucleated inclusions and particulates responsible for the ductile fracture behavior in conventional metals, as well as the much larger AM porosity generated by defects formed during the additive manufacturing process. In traditional modeling of ductile fracture in conventional metals, the background porosity is often implicitly modeled using Gurson computational cells within a refined mesh region directly ahead of the crack notch-tip. The Gurson model, later extended by Tvergaard and Needleman, is a phenomenological model that predicts the behavior of an elastoplastic material containing nucleating voids which grow and coalesce (Chu & Needleman, 1980; Gurson, 1977; Tvergaard, 1982). The Gurson model considers the constitutive response of a cell of size D containing a spherical void at its center (Fig. 2.3) with an initial void volume fraction of f_0 within a solid matrix material of initial volume fraction $(1 - f_0)$.

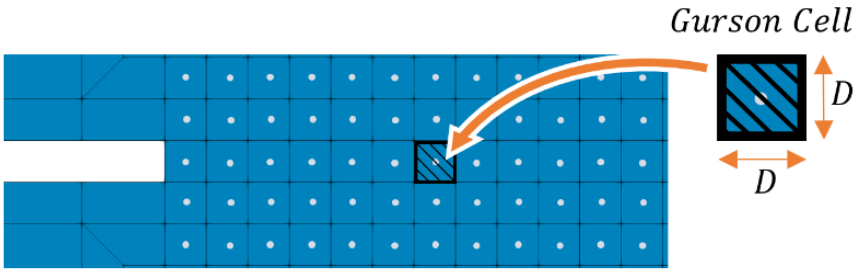

Figure 2.3. *Gurson cell representation of background porosity within the FPZ*

The porosity or void volume fraction f increases with load and leads to a gradual loss of stress carrying capacity in a macroscopic material element once the extinction void volume fraction f_E is reached. Upon reaching f_E, the Gurson element invokes extinction and is "*killed*" by enforcing tractions being reduced to zero over a user defined number of subsequent load steps. In this investigation, tractions post-extinction were gradually reduced over 10 load steps. Employing strain hardening in conjunction with the Gurson model allows a material to yield, strain harden, soften, and rapidly fracture (Fig. 2.4). While the Gurson model has been augmented to allow for the nucleation of voids once a critical strain level is reached (Chu & Needleman, 1980), these strain levels are relatively low compared to the strains needed for void coalescence. In this thesis, the background voids in AM Ti-6Al-4V are assumed to be pre-existing.

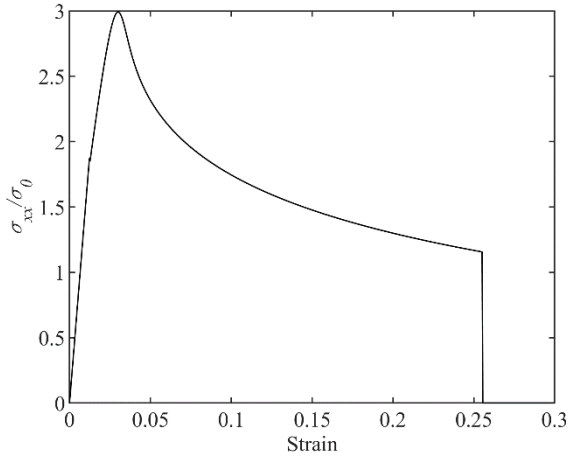

Figure 2.4. *Stress-strain response for a single Gurson cell undergoing uniaxial straining*

The Gurson yield condition is given by

$$\Phi(\sigma_e, \sigma_m, \bar{\sigma}, f) = \left(\frac{\sigma_e}{\bar{\sigma}}\right)^2 + 2q_1 f cosh\left(\frac{3q_2\sigma_m}{2\bar{\sigma}}\right) - (1 + q_3 f^2) = 0 \quad (2.3)$$

where σ_e denotes the (Mises) equivalent stress, σ_m is the mean (macroscopic) stress, $\bar{\sigma}$ is the (Mises) equivalent stress of the matrix material surrounding the phenomenological void and f is the current void fraction. Modulating the three coefficients, (q_1, q_2, q_3) was found to improve the model predictions for periodic arrays of Gurson cells, each containing a spherical void and where $q_3 = q_1^2$ (Tvergaard, 1982). It has been shown that these q parameters have a strong dependency on the ratio of yield strength to Youngs' modulus, $\frac{\sigma_0}{E}$, and the strain hardening parameter, N (Faleskog et al., 1998). The conventional alloy in this thesis is assumed to be wrought Ti-6Al-4V (Shunmugavel et al., 2015) with a Young's modulus of 107 GPa, yield strength of 940 MPa, Poisson's ratio of 0.3, and a strain hardening exponent of N = 0.04. The q_1 and q_2 parameters used in this investigation were 1.242 and 1.113, respectively, and were determined by linearly extrapolating from suggested values in Table 2.1 for Ti-6Al-4V with parameters $\frac{\sigma_0}{E} = 0.0089$ and strain hardening exponent N = 0.04.

Table 2.1. Suggested values for q_1 and q_2 (Faleskog et al., 1998)

	$\frac{\sigma_0}{E} = 0.001$		$\frac{\sigma_0}{E} = 0.002$		$\frac{\sigma_0}{E} = 0.004$	
Hardening, N	q_1	q_2	q_1	q_2	q_1	q_2
0.025	1.88	0.956	1.84	0.977	1.74	1.013
0.050	1.63	0.950	1.57	0.974	1.48	1.013
0.075	1.52	0.937	1.45	0.960	1.33	1.004
0.1	1.58	0.902	1.46	0.931	1.29	0.982
0.15	1.78	0.833	1.68	0.856	1.49	0.901
0.2	1.96	0.781	1.87	0.800	1.71	0.836

This numerical model strives to be the digital twin of AM Ti-6Al-4V with similar AM void frequencies and void diameters as that in actual AM specimens (Foehring et al., 2018). Cross-sectional optical micrographs (Fig. 2.5) of AM Ti-6Al-4V were collected to study the distribution of AM void diameters. A previously tested AM tensile specimen from Foehring et al. (2018) was mounted in epoxy and

polished following the procedure in Table 2.2. Optical microscopy was performed on 5 cross-sectional slices of the specimen grip section (to minimize any effects of the loading history that the sample had undergone) and distributions of AM void diameters and nearest neighbor distances were recorded (Fig. 2.6).

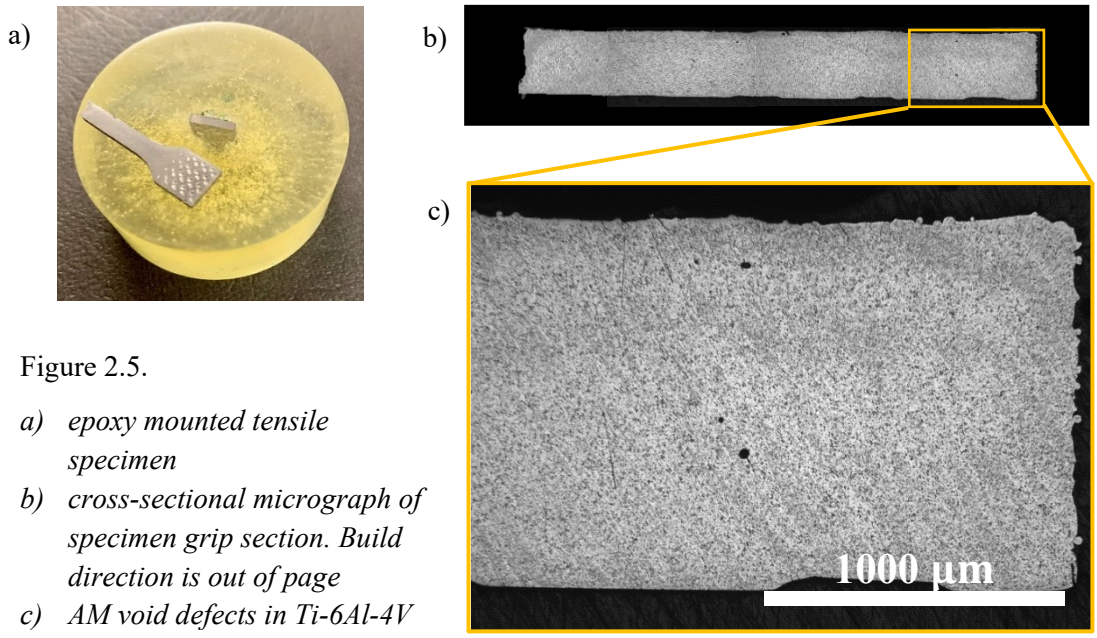

Figure 2.5.

a) epoxy mounted tensile specimen
b) cross-sectional micrograph of specimen grip section. Build direction is out of page
c) AM void defects in Ti-6Al-4V

Table 2.2. Polishing procedure for AM Ti-6Al-4V cross-sectional micrographs

Step	Type	Paper/Pad	Compound	Lubricant	Contra-rotation
1	Grinding	320 grit (P400) Silicon Carbide	N/A	Tap Water	No
2	Grinding	600 grit (P400) Silicon Carbide	N/A	Tap Water	No
3	Grinding	800 grit (P400) Silicon Carbide	N/A	Tap Water	No
4	Grinding	1200 grit (P400) Silicon Carbide	N/A	Tap Water	No
5	Polishing	Buehler Ultra-Pad	9µm diamond	DI Water	Yes

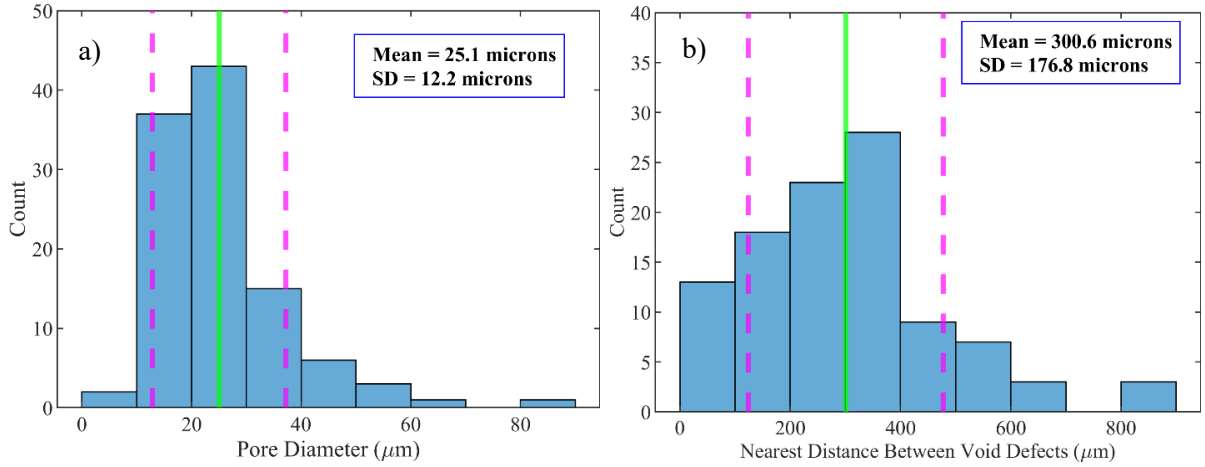

Figure 2.6. *a) AM defect diameters and b) nearest neighbor distances from AM Ti-6Al-4V specimen*

One possible source of these AM void defects is from the incomplete, or in some cases entirely, un-melted metal powder particles. The distribution of AM metal powder particle diameters for the Ti-6Al-4V specimen was quantified (Fig. 2.7) and the average metal powder particle was determined to be about 20 µm. Combining these results led to selecting AM voids of 20 µm in diameter in the numerical model.

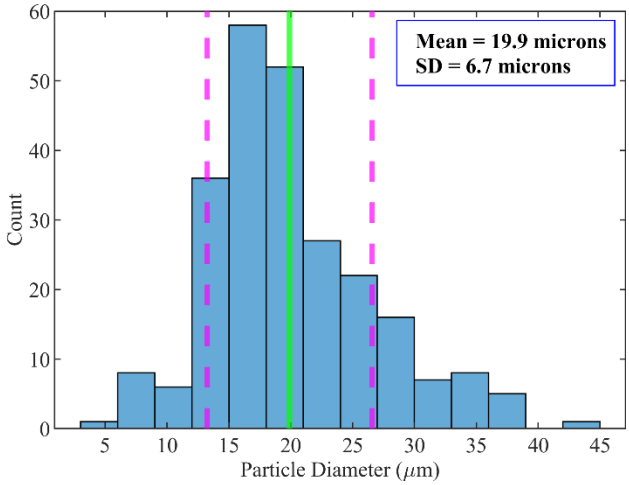

Figure 2.7. *Ti-6Al-4V additive manufacturing powder particle diameter distribution*

Modeling the ductile fracture process implicitly using Gurson computational cells within the FPZ introduces an intrinsic length-scale governed by the Gurson element size, D (Gao et al., 1998; Xia & Shih, 1996). Conventionally, D is interpreted to be the size of a material cell containing one inclusion or background pore. In this study, D was chosen to be 16 µm, as a 16 µm × 16 µm × 16 µm cube occupies

approximately the same void volume as a typical spherical AM void defect with a diameter near 20 μm (Fig. 2.6) and because powder particles also tend to be about ~16 μm in diameter (Fig. 2.7).

To differentiate between the two size-scales of voids in AM metals, the implicitly modeled initial background porosity is referred to as f_0, while the AM void porosity is referred to as V_f.The average nearest neighbor distance, in conjunction with the average AM void diameter in our AM Ti-6Al-4V specimen, was used to find AM void defect frequencies of interest. To calculate an expected AM void defect volume fraction, the total volume of all AM defects was divided by the volume formed by the area of the optical micrographs times the average nearest AM void distance (assumed to be the same in all directions). The AM void defect volume fraction was determined to be $V_f = 0.0002$ through this method, in line with expectations for a high quality, highly dense AM material (Liu & Shin, 2019). When this low AM void defect fraction is added to a material's background porosity, in this study $f_0 = 0.005$, it produces an effective material density of 99.48%, in accordance with the AM alloys manufactured using the optimal additive manufacturing process parameters as advertised by manufacturers of additive manufacturing machines (*Get the Facts On… Porosity in Metal Additive Manufacturing | GE Additive*, 2021). Therefore, it was decided to keep AM void defects to low volume fractions (less than a V_f = 0.02 AM void volume fraction) in an attempt to model highly dense AM products that are up to 99.5% dense.

Table 2.3 summarizes the material properties used in this investigation. The initial background porosity was chosen as $f_0 = 0.005$ considering the Gurson parameters (q_1, q_2, q_3) recommended in Faleskog et al. (1998), which were linearly extrapolated for Ti-6Al-4V in this study, were calibrated using a porosity range of $0.001 \leq f_0 \leq 0.01$. Although f_0 has historically been used as a fitting parameter (Gao et al., 1998), in this case f_0 also takes on a microstructural basis. At $f_0 = 0.005$, each Gurson cell with side length D = 16 μm represents a spherical pore 3.4 μm in diameter, falling within the expected range (2-12 μm) of small-scale pore diameters (Cui et al., 2020).

Table 2.3. Summary of material properties in numerical simulations

E (GPa)	σ_0 (MPa)	ν	N	q_1	q_2	q_3	D (μm)	f_0	f_E
107	940	0.3	0.04	1.242	1.113	1.543(=q_1^2)	16	0.005	0.2

2.3. AM Void Representation

AM defects present in AM Ti-6Al-4V are mostly spherical, with a few instances of elliptical voids or clustered groups of voids observed in optical micrographs (Fig. 2.5). However, modeling AM defects as discrete spherical voids can be numerically challenging and computationally expensive, particularly in 3D MBL models containing a large number of such AM voids within the process zone. Instead, here an AM void defect is modeled explicitly by deleting a single cubic Gurson cell directly from the pre-existing FPZ mesh (Fig. 2.8 in 2D and Fig. 2.9 in 3D).

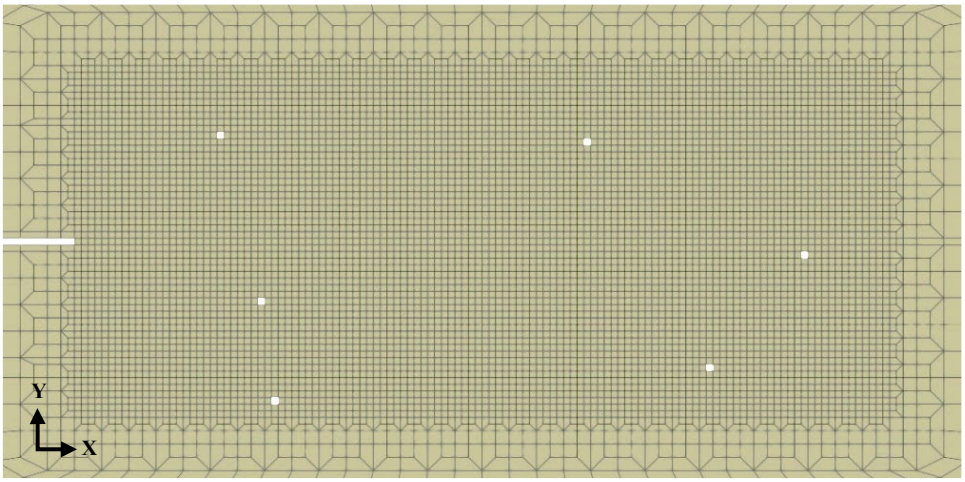

Figure 2.8. *AM void defects are represented by removing Gurson cells from mesh*

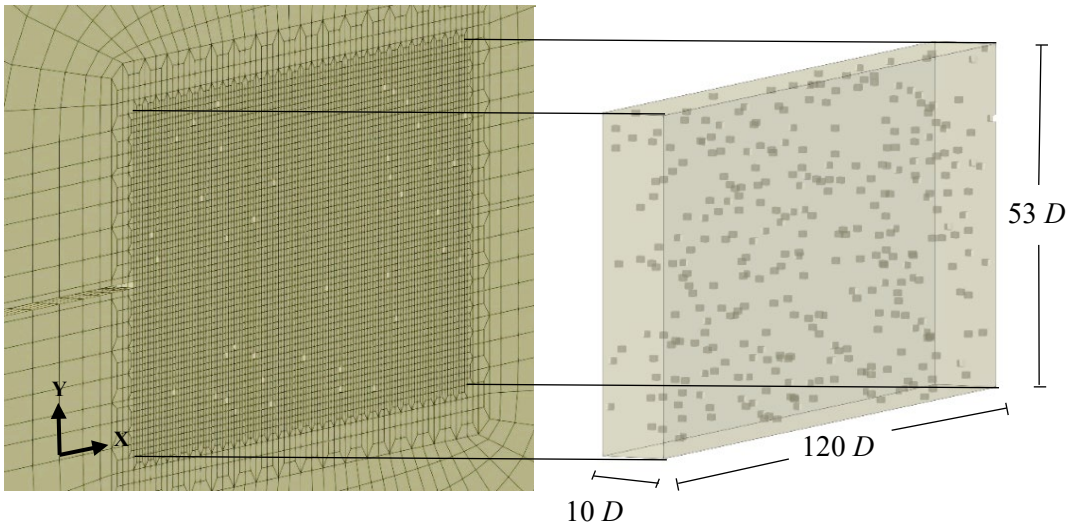

Figure 2.9. *3D model with AM void defects represented by single cells deleted from the mesh*

In the past, void growth under physical states similar to those found in the highly stressed regions ahead of a crack have been studied through the use of representative volume elements (RVEs) (Faleskog & Shih, 1997). To verify the modeling simplification of using cubic rather than spherical voids in the FPZ, a unit cell study was conducted comparing the stress-strain, porosity, and stress triaxiality evolution for cubic and spherical void RVEs with different initial void volume fractions, V_f. Finite element $1/8^{th}$ unit cell models (Fig. 2.10) were created, each containing either a spherical or cubic void, using the same elastoplastic material properties as for our MBL model. Finite strain deformation was used in these verification analyses. The RVEs were subjected to uniaxial straining and uniaxial tension loading conditions (Fig. 2.11). Under uniaxial straining, only displacements along the axial direction ($+x$-axis) were permitted. Under uniaxial tension, displacements were also applied along the $+x$-axis while the lateral surfaces of the unit cell were free to move and were under a multi-point constraint to maintain a prismatic unit cell regardless of load. Initial void volume fractions, V_f, studied were 0.004, 0.05, 0.1, 0.15, and 0.2.

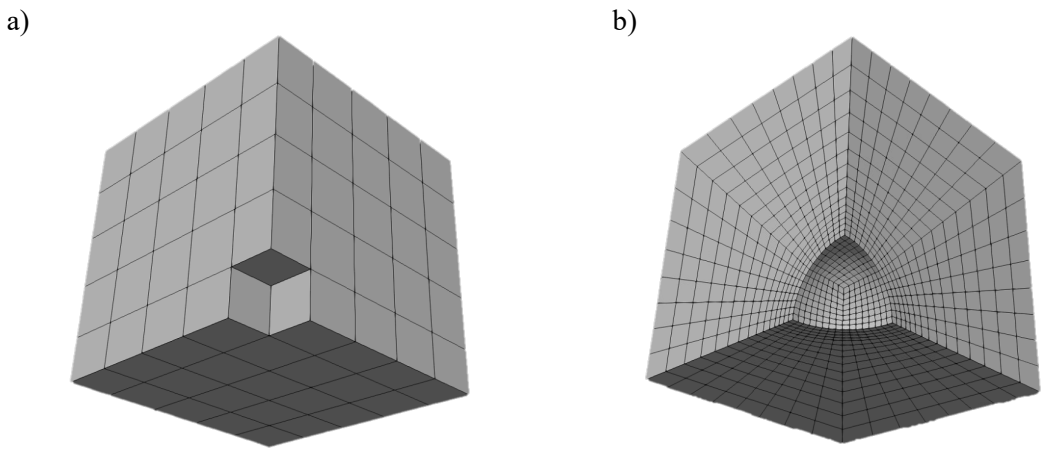

Figure 2.10. *1/8th unit cell meshes for a) cubic void and b) spherical void RVEs*

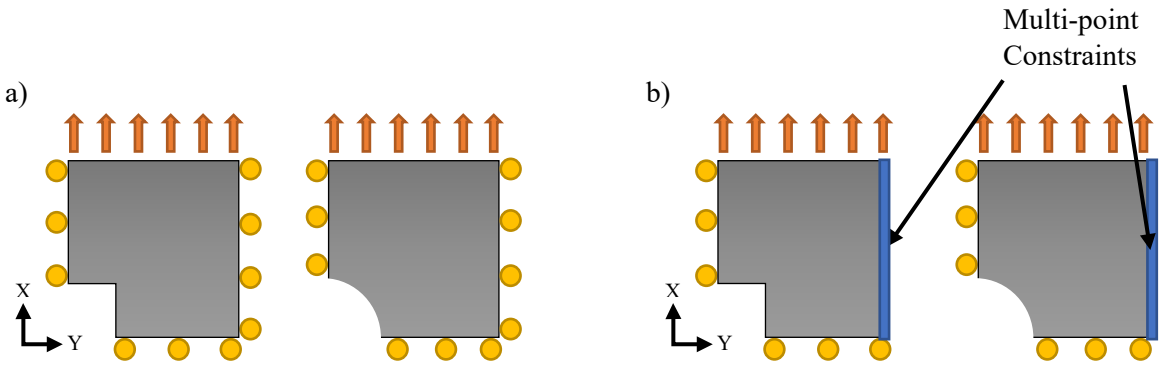

Figure 2.11. *a) Uniaxial straining conditions and b) uniaxial tension loading conditions*

The porosity evolution was found to be nearly identical between the RVEs with spherical and cubic initial void shapes under both loading conditions for all V_f tested (Fig. 2.12). Similarly, axial stress (σ_{xx}) compared well between the cubic and spherical void representations, with the uniaxial tension response being nearly identical between the cubic and spherical void representations for all values of V_f. Under uniaxial strain bounds however, the stress-strain response begins to deviate with increasing void volume fraction, potentially due to low triaxiality levels present in the laterally unconstrained uniaxial tension analysis (Fig. 2.13).

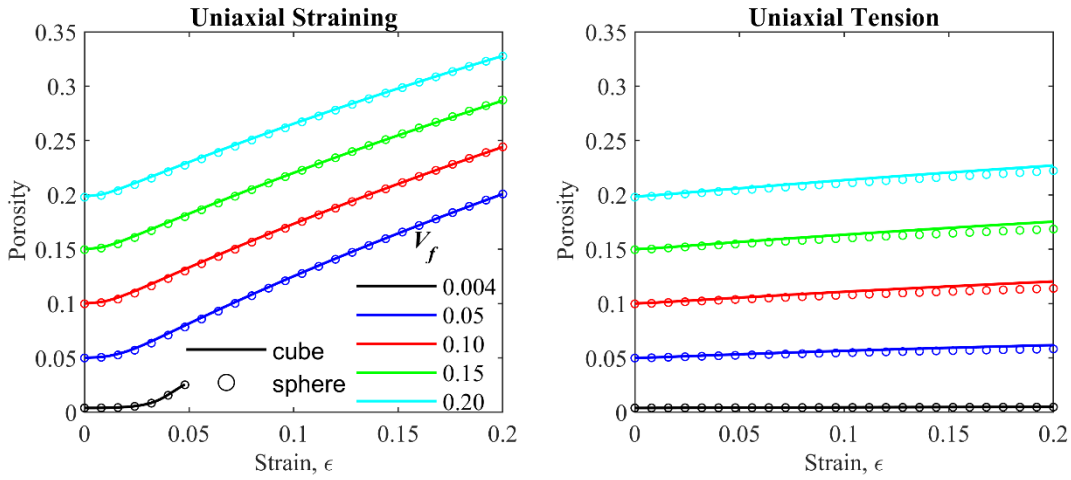

Figure 2.12. *RVE porosity as a function of strain for increasing initial V_f under uniaxial strain and uniaxial tension loading conditions*

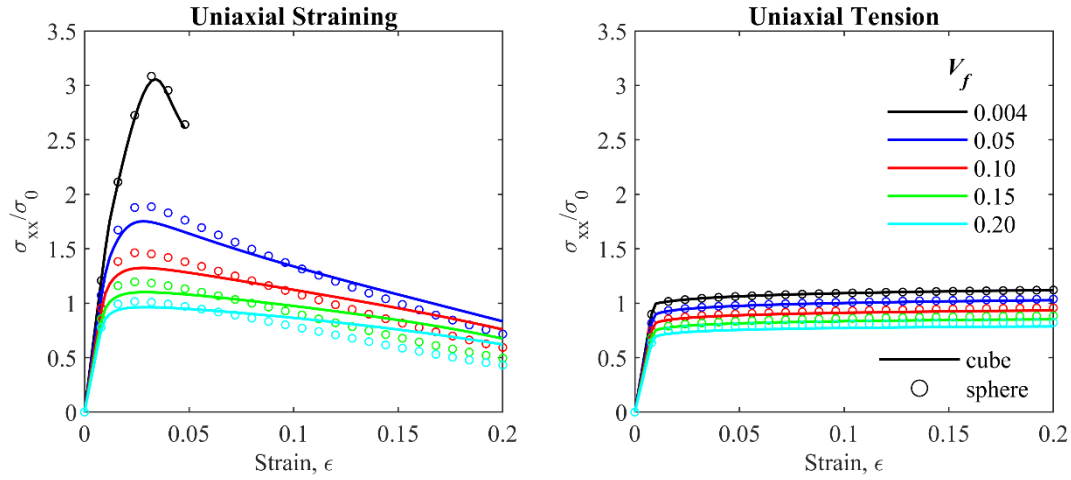

Figure 2.13. *RVE axial stress as a function of strain for increasing initial V_f under uniaxial strain and uniaxial tension loading conditions*

The same trend is evident when plotting axial stress (σ_{xx}) against the RVE porosity, where the effects of stress triaxiality are seen in the significantly greater void growth for uniaxial strain conditions (Fig. 2.14).

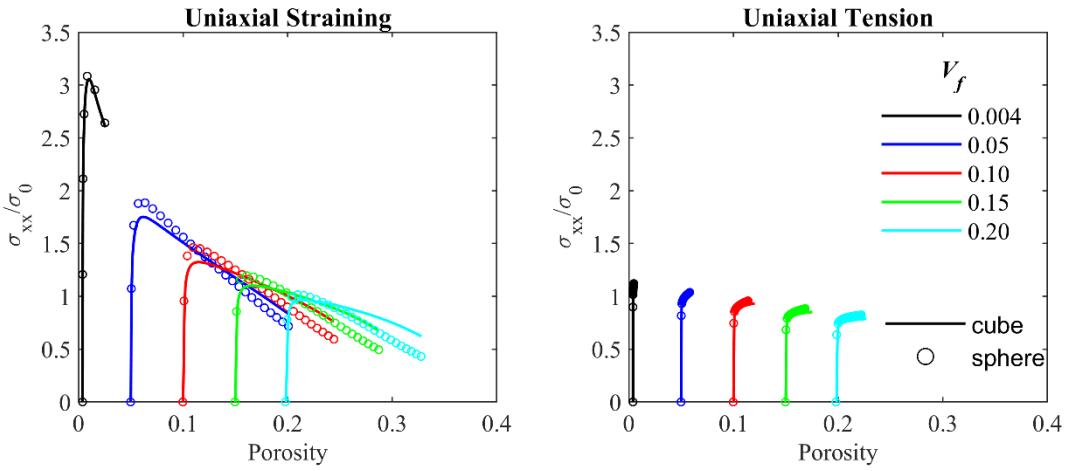

Figure 2.14. *RVE axial stress as function of current porosity for increasing initial V_f under uniaxial strain and tension loading conditions*

To capture the differences between cubic and spherical void RVEs under a triaxial stress state, the Triaxiality Factor (T.F.) was calculated for increasing initial V_f under uniaxial strain loading conditions. The triaxiality factor is defined as the ratio of mean stress (σ_m) to equivalent stress (σ_e) (Eq. 2.4).

$$T.F. = \frac{\sigma_m}{\sigma_e} = \frac{\frac{1}{3}(\sigma_{11}+\sigma_{22}+\sigma_{33})}{\sqrt{\frac{(\sigma_{11}-\sigma_{22})^2+(\sigma_{22}-\sigma_{33})^2+(\sigma_{33}-\sigma_{11})^2+6(\sigma_{13}^2+\sigma_{23}^2+\sigma_{31}^2)}{2}}} \tag{2.4}$$

Cubic void unit cells exhibited significantly lower triaxiality factors as the RVE porosity increased (Fig. 2.15). The triaxiality factor evolution also lacked an inflection point past the initial void fraction $V_f = 0.05$, where triaxiality appears to plateau and decrease as the current RVE porosity increases in larger initial V_f. This mismatch in the RVEs at large initial V_f taken in conjunction with the known shortcomings of the Gurson model, which overpredicts failure strain under low stress triaxiality, allows us to select $V_f = 0.05$ as an upper bound on the largest void volume fractions permitted though this AM void representation in the FPZ. Smaller initial AM void defect volume fractions under 0.05 ($V_f \leq 0.05$) using a cubic void representation appears to be an acceptable substitute for modeling spherical defects in AM Ti-6Al-4V.

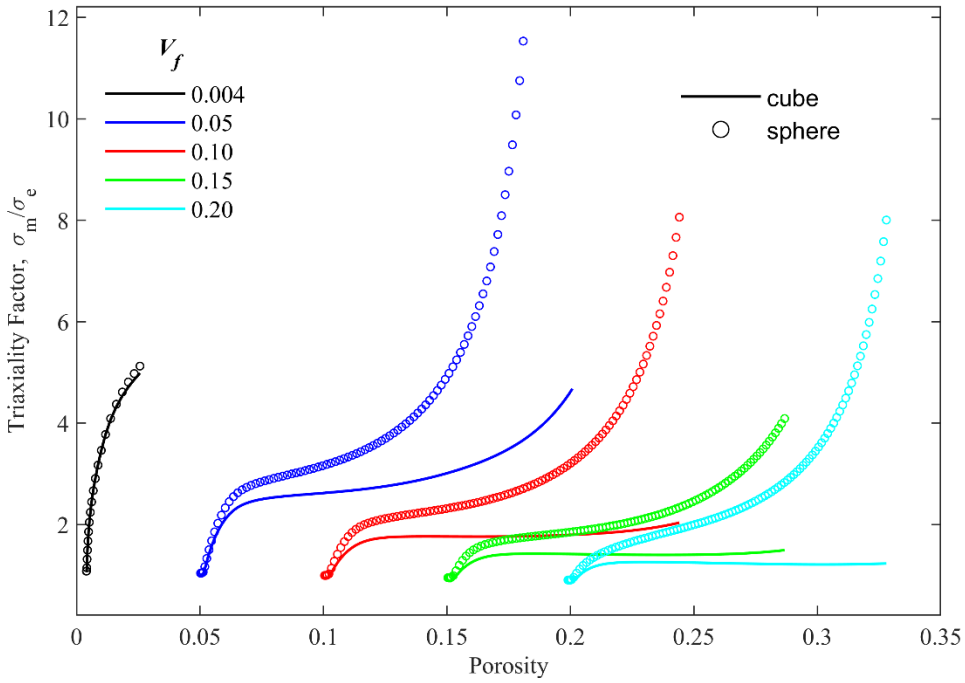

Figure 2.15. *Triaxiality factor versus porosity of RVEs under uniaxial strain loading conditions*

CHAPTER 3 – CRACK-DEFECT INTERACTIONS

3.1. Background Porosity in Conventional Ti-6Al-4V

3.1.1. 2D Modeling

The intrinsic background porosity within the FPZ is modeled with Gurson cell elements with initial porosity, f_0. Fig. 3.1 shows the fracture resistance curves (*R*-curves) of 2D plane strain models for conventional Ti-6Al-4V alloys with no additive manufacturing process defects and with background porosities of f_0 = 0.0025, 0.005, 0.0075, and 0.01. The *J*-integral is unambiguously related to the applied K_I stress intensity factor by

$$J = \frac{K_I^2}{\bar{E}} \tag{3.1}$$

where $\bar{E} = \frac{E}{1-\nu^2}$ or E under plane strain or plane stress conditions, respectively, E is the Young's modulus, and ν is the Poisson's ratio. In both 2D and 3D models, the crack extension (Δa) was calculated as a the projected length along the *x*-axis at the mid-plane of the model ($z = 0\ D$), where crack length is longest in 3D models because of crack tunneling, and is normalized by the Gurson cell size, *D*. For each load step, as Gurson cells in front of the propagating crack tip reached the extinction porosity ($f_E = 0.2$) and coalesced with the crack front, the crack length and crack tip position were updated. Isolated damage zones (regions ahead of the main crack which have already failed but have not yet coalesced with the main crack) were included in the crack length measurement only once they were within two Gurson cells from joining the main crack in an attempt to measure only contiguous crack growth. In 2D models, *R*-curves depict a seemingly brittle response for all f_0, and quickly reach a steady-state toughness. Results show that decreasing the background porosity increases both the fracture initiation toughness Γ_0, and the steady-state fracture toughness Γ_{ss} responsible for unstable crack propagation. Note that Γ_{ss} for the lowest porosity modeled, f_0 = 0.0025 is nearly twice that for all other background porosities modeled, with Γ_{ss} values decreasing monotonically with increasing f_0 but approaching a saturation limit.

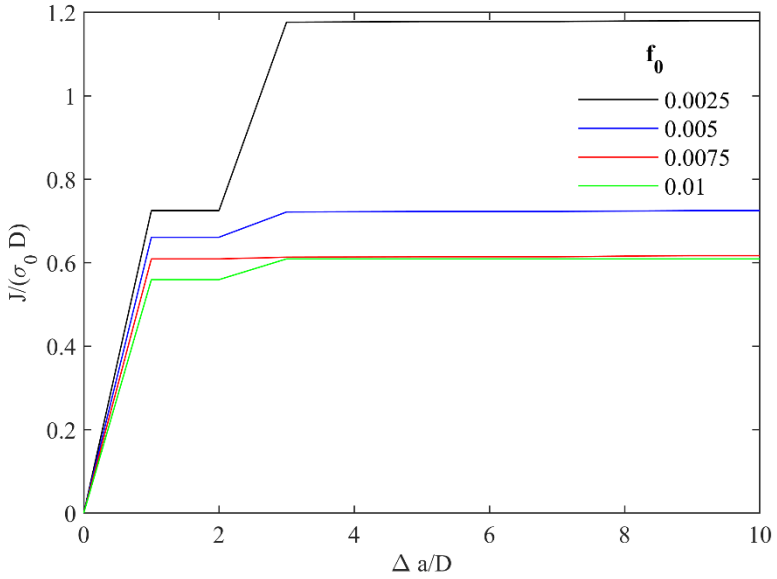

Figure 3.1. *R-curves for conventional Ti-6Al-4V 2D plane strain models with increasing background porosity*

The increase in fracture initiation toughness ($\Delta\frac{a}{D} = 1$) with decreasing f_0 is accompanied by an increase in the plastic zone, operationally defined by accumulated plastic strain, $\epsilon_p \geq 0.001$ (Fig. 3.2). The shape of the plastic zone evolves from an elongated profile to become more butterfly-like with a reduction in f_0, which effectively reduces the spread of the plastic zone directly ahead of the notch-tip.

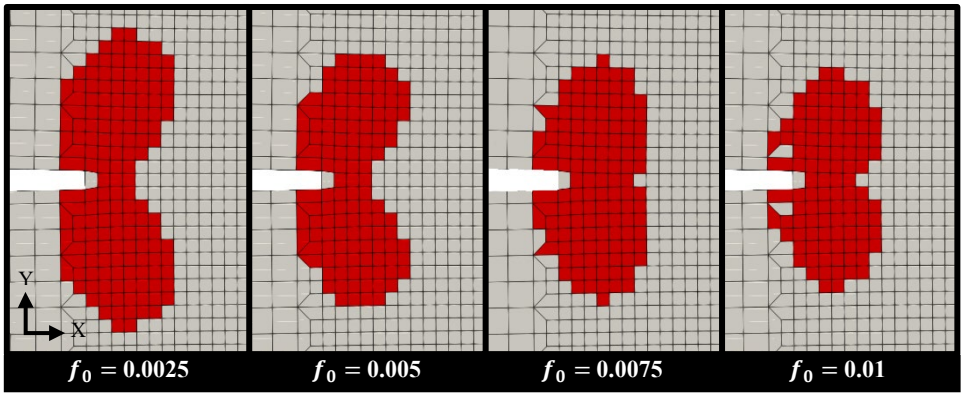

Figure 3.2. *Accumulated plastic strain contours for $\epsilon_p \geq 0.001$ in 2D models with increasing background porosity*

3.1.2. 3D Modeling

A similar study of the effects of background porosity on the fracture initiation toughness and the plastic zone size was performed for 3D models of conventional Ti-6Al-4V with no AM void defects. As in 2D models, the fracture initiation toughness Γ_0 consistently decreases with increasing f_0 (Fig.3.3), though these values were generally lower for the 3D analyses, except when f_0 = 0.01 (i.e., near the limiting saturation value seen in Fig. 3.1) where the Γ_0 values were similar. The full fracture resistance *R*-curves from the 3D simulation results, however, tell a different story (Fig. 3.4).

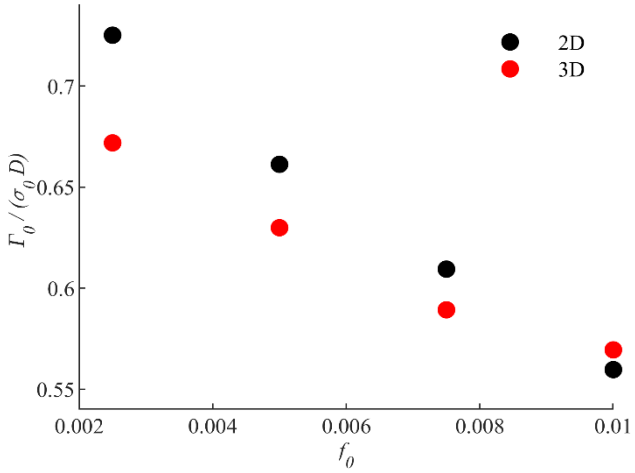

Figure 3.3. *Fracture initiation toughness for conventional Ti-6Al-4V with increasing background porosity*

Unlike 2D models where the *R*-curves tend to saturate soon after crack initiation, suggesting limited plastic dissipation in the background material, *R*-curves for the 3D models steadily increase with crack advance. This more stable fracture response of the 3D models allowed for stable crack propagation even up to $\Delta a = 80D$, confirming the need for 3D analysis for accurate fracture response modeling. On this note, the fracture toughness of conventional Ti-6Al-4V ranges from K_{IC} of 84 to 110 MPa$\sqrt{\text{m}}$ (Becker et al., 2015; *Titanium Alloys - Ti6Al4V Grade 5*, 2002; Van Hooreweder et al., 2012). Considering the typical spacing of ~16 μm between particles or inclusions in the background material which is the very definition of the Gurson element size D in our 3D model, this translates to a normalized fracture toughness value of

$J/(\sigma_0 D)$ between 3.99 and 6.84 for conventional Ti-6Al-4V, which falls between the fracture initiation and steady-state $J/(\sigma_0 D)$ obtained in our 3D finite element simulations for the range of f_0 values considered. This confirms the accuracy of the 3D model in quantitatively capturing the fracture toughness response of conventional Ti-6Al-4V alloys.

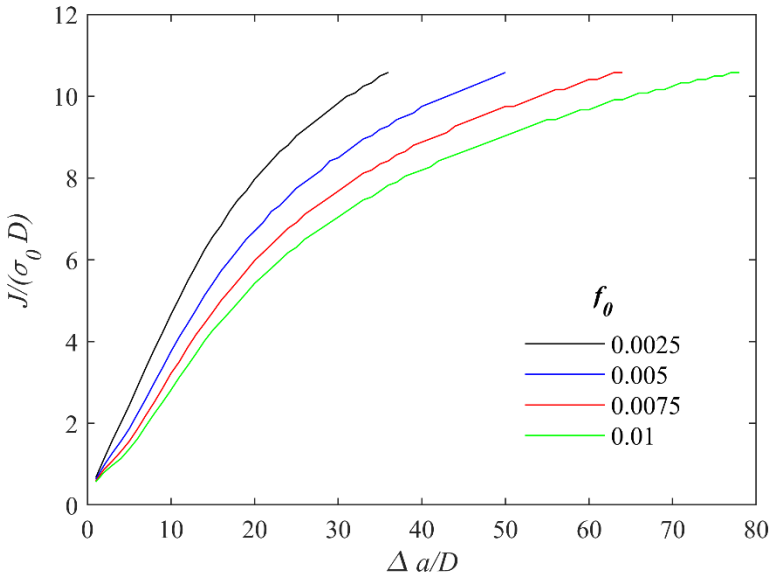

Figure 3.4. *R-curves for conventional Ti-6Al-4V 3D models with increasing background porosity*

For completeness, Figs. 3.5-3.6 show cross-sectional views of the plastic strain region (operationally defined by accumulated plastic strain $\epsilon_p \geq 0.001$) just after crack initiation along $z = 0$ D and $z = 10$ D representing the mid-plane and free surface of the 3D model, respectively. Similar to the 2D models, the plastic zone size for the 3D models decreases with increasing f_0. The plastic zone at the free surface representing plane stress conditions is slightly larger than the plastic zone along the mid-plane representing plane strain conditions. This suggests the transition from plane stress to plane strain begins within the thickness of the model and can also be seen in the oblique view of the plastic zone contours in Fig. 3.7.

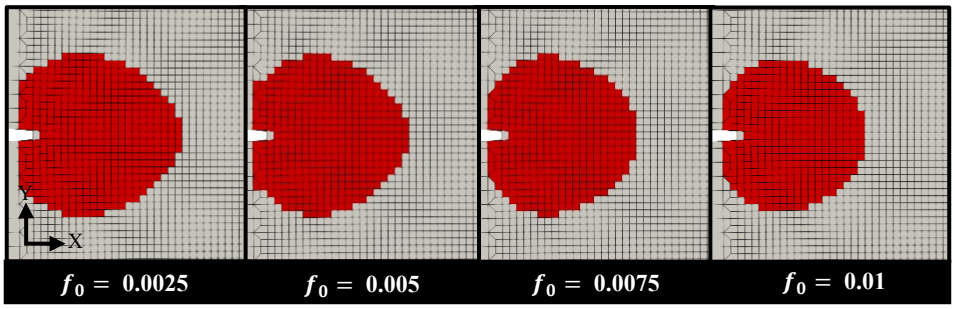

Figure 3.5. *Mid-plane accumulated plastic strain contours where $\epsilon_p \geq 0.001$ in 3D models without AM void defects for increasing f_0*

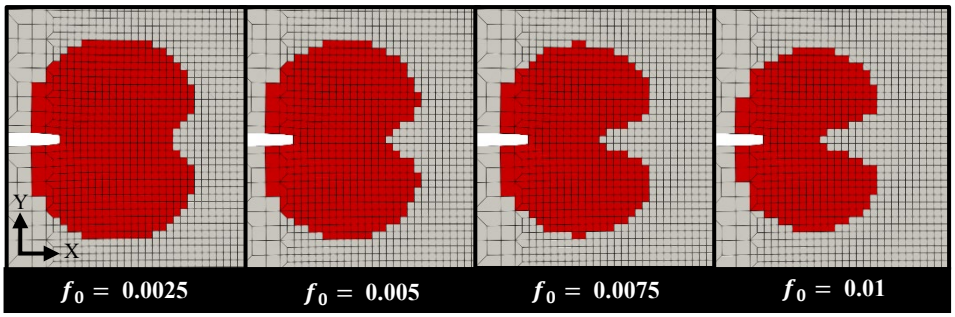

Figure 3.6. *Free surface accumulated plastic strain contours where $\epsilon_p \geq 0.001$ in 3D models without AM void defects for increasing f_0*

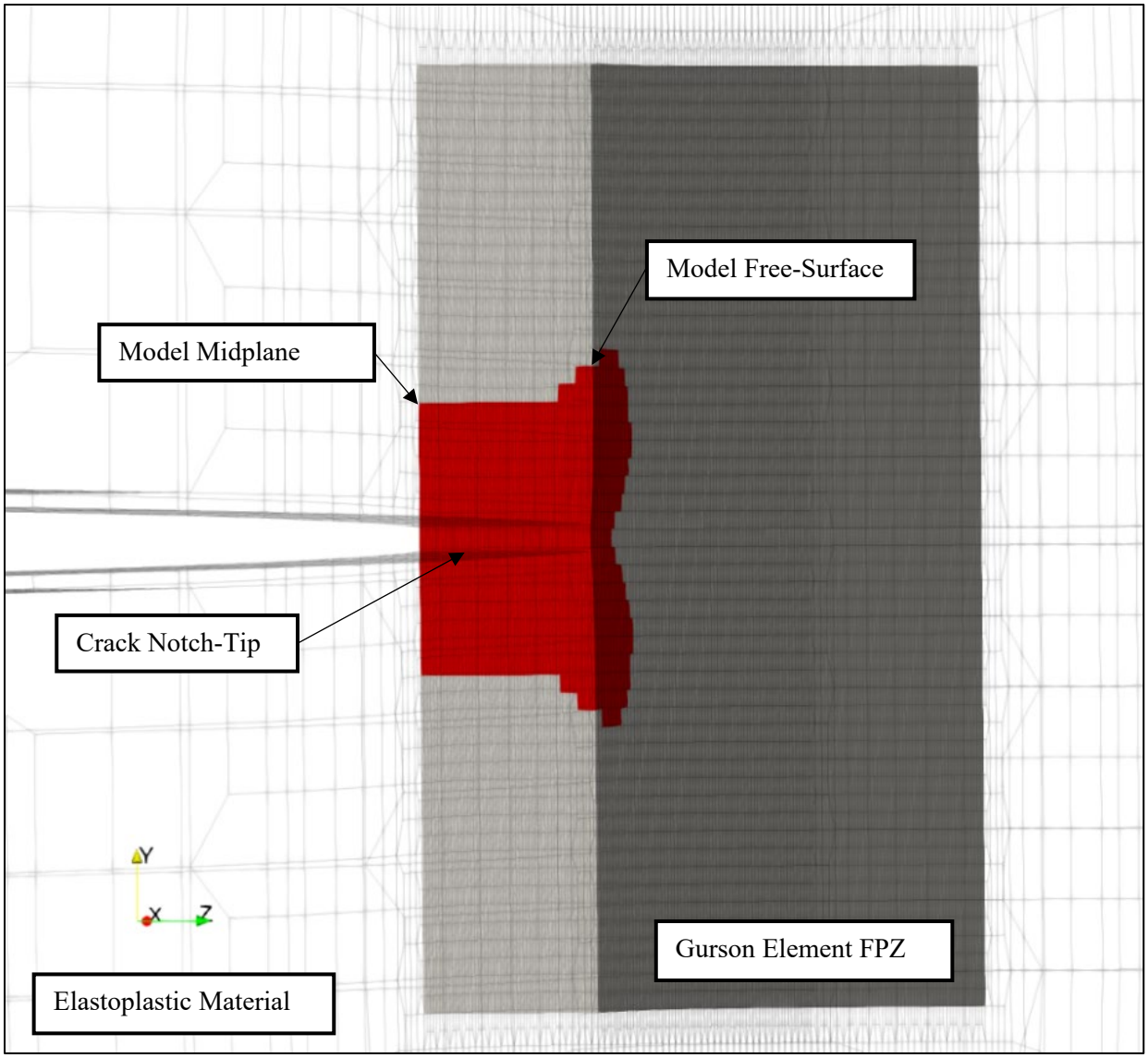

Figure 3.7. *Accumulated plastic strain ($\epsilon_p \geq 0.001$) showing the start of the plastic zone transition from plane stress to plane strain ahead of the notch-tip in 3D models with no AM void defects and $f_0 = 0.005$*

3.2. Damage Mechanisms of AM Void Defects

3.2.1. 2D Modeling

Unlike conventional Ti-6Al-4V, AM Ti-6Al-4V builds contain additive manufacturing process defects in the form of large voids (average diameter 20-30 μm) as compared to the smaller and uniformly-distributed background porosity represented in our models via Gurson cell elements. Fig. 3.8 compares the von Mises stress fields at indentical K_I loading between the 2D modeling of conventional (Fig. 3.8a) versus AM-produced Ti-6Al-4V containing an initial AM void defect volume fraction of V_f = 0.005 within the crack-tip process zone (Fig. 3.8b) Results show the development of high localized stress concentrations around each AM void defect, especially near the active crack-tip plastic zone.

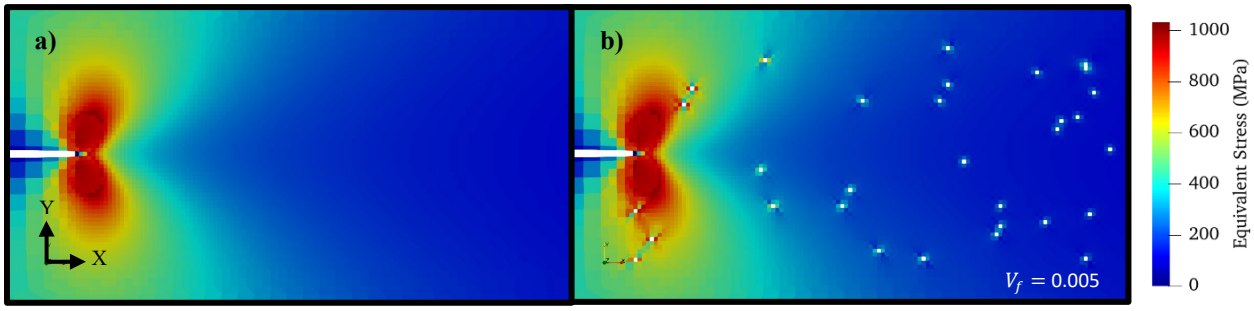

Figure 3.8. *Von mises stress fields (Equivalent Stress) ahead of crack tip for a) Ti-6Al-4V without and b) with AM void defects*

To better understand the effects of void placement on fracture toughenss in the 2D models, the *R*-curves for ten instantiations of AM void defects were independently generated for each of the initial AM void fractions of $V_f = 0$, 0.001, and 0.005 (Fig. 3.9). While the presence of AM voids did not change the fracture initiation toughness, a number of AM models (labeled as #1 and #2 in Fig. 3.9) display remarkably higher steady-state fracture toughness compared to the conventional material without AM voids. All models however, attain a steady state toughness values soon after fracture initiation.

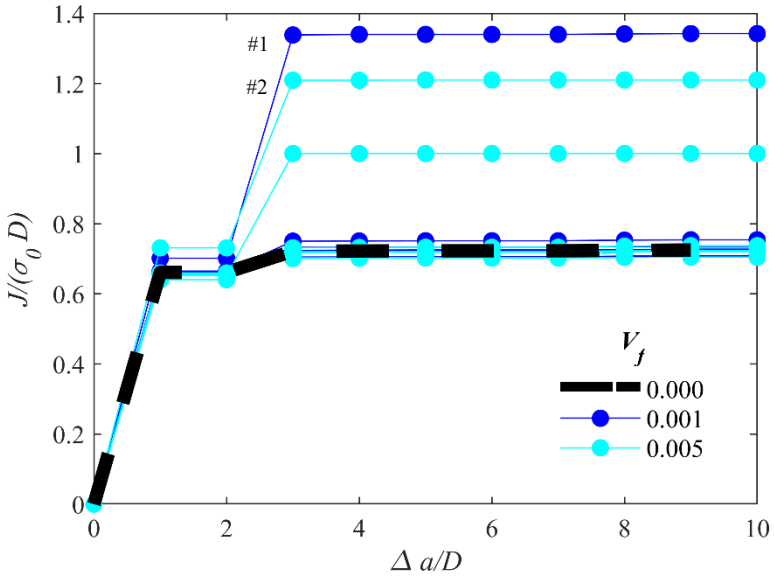

Figure 3.9. *R-curves for AM Ti-6Al-4V 2D models with random instantiations of AM void defects*

To elucidate the above damage response in the presence of AM void defects, we compare in Figs. 3.10-3.14 contours of the porosity distribution and plastic strain zones (operationally defined by accumulated plastic strain $\epsilon_p \geq 0.001$) at a fixed crack extension of $\Delta\frac{a}{D} = 10$. In the 2D model for conventional Ti-6Al-4V, damage is confined to a narrow band of Gurson cells directly ahead of the crack-tip, resulting in a straight crack-path with a symmetrical plastic wake. The background voids outside of this single-element-thick narrow process zone do not undergo appreciable void growth. This damage response resembles those modeled by the cell element approach of Xia & Shih (1995) and Faleskog et al., (1998), which utilized only a single row of Gurson cell elements to capture the failure mechanism of the FPZ.

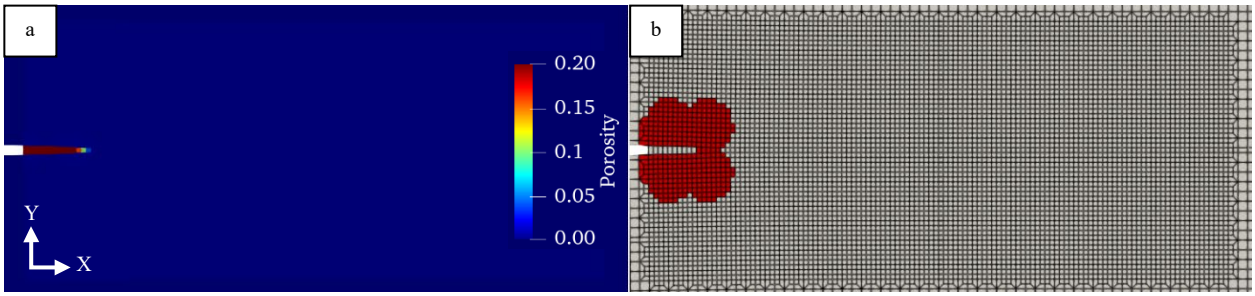

Figure 3.10. *a) Porosity and b) accumulated plastic strain ($\epsilon_p \geq 0.001$) contours of 2D conventional Ti-6Al-4V at $\Delta a/D = 10$*

In the presence of AM defects at void fraction V_f = 0.001, model #1 displayed the highest steady-state fracture toughness in Fig. 3.9 and a clear deflection of the crack path towards an AM void defect in Fig. 3.11a, along with a much larger plastic wake (Fig. 3.11b) versus the conventional metal (Fig. 3.10b) or a "reference" AM material with voids present further away from the crack tip so that they do not interact as much with it (Fig. 3.13b).

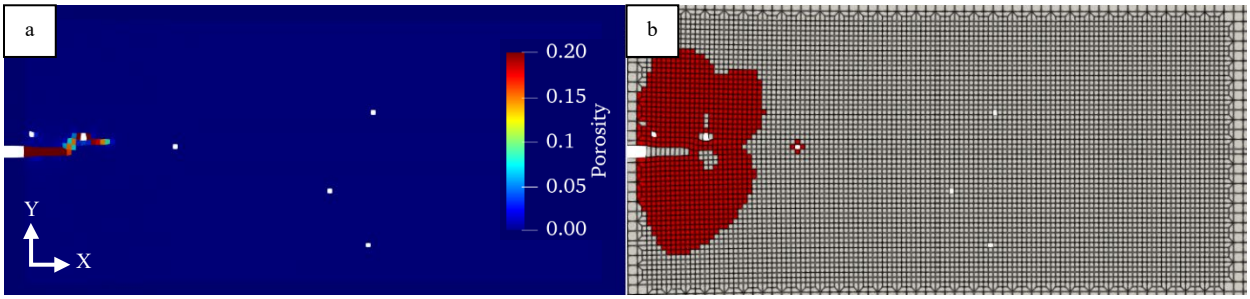

Figure 3.11. *2D Model #1 from Fig. 3.9 with above-average fracture response: a) porosity and b) accumulated plastic strain ($\epsilon_p \geq 0.001$) with V_f = 0.001 at* Δ *a/D* = 10

Similar observations were made for model #2 which had a higher AM void volume fraction, V_f = 0.005, and exhibited comparable steady-state fracture toughness levels to model #1 (Fig. 3.9). The porosity and plastic strain contours show a clear deflection of the crack path towards a cluster of AM void defects in model #2, and resulted in a larger, and more fragmented plastic wake which appeared to be split into two distinct zones: the first at the original notch-tip, and the second centered at a confluence of three AM void defects located at ~45° below the notch-tip (Fig. 3.12).

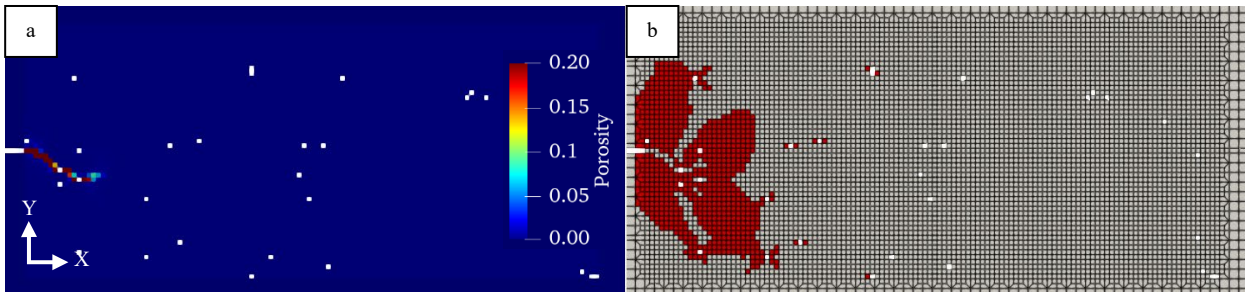

Figure 3.12. *2D Model #2 from Fig. 3.9 with above-average fracture response: a) porosity and b) accumulated plastic strain ($\epsilon_p \geq 0.001$) with V_f = 0.005 at* Δ *a/D* = 10

These results suggest that the strategic placement of the AM voids near the initial notch-tip in both models #1 and #2 resulted in significant crack path deviation and crack-tip blunting to cause the larger and more diffuse plastic wakes, which account for the higher steady-state fracture toughness. We note that not all AM void placements result in crack-tip toughening or crack tortuosity. Figs. 3.13-3.14 show the porosity and plastic strain contours for the "typical" or more common fracture toughness response of AM models with void fractions of $V_f = 0.001$ and $V_f = 0.005$, respectively. While these AM void fractions are the same as in models #1 and #2, both these model structures had no AM voids near or along the crack path, resulting in similar plastic strain and fracture response to conventional Ti-6Al-4V. It is important to note that all four AM models discussed exhibited yielding around AM voids ahead of the main plastic zone, leading to potential increased energy dissipation over conventional Ti-6Al-4V, and therefore potential for increased local toughness.

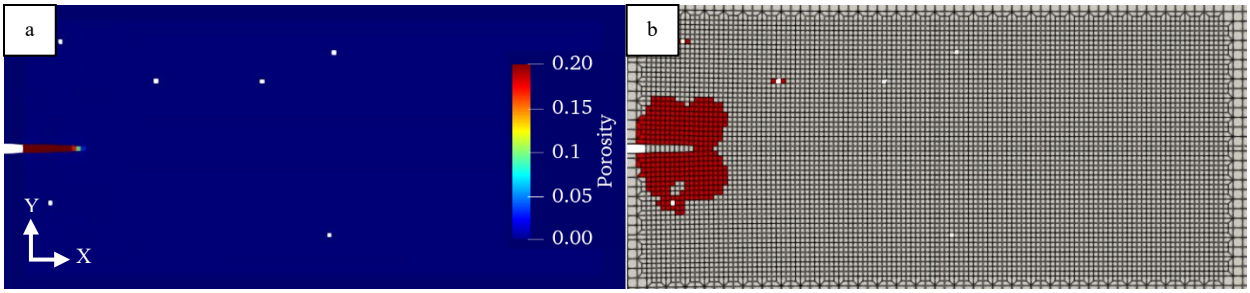

Figure 3.13. *Reference model for V_f = 0.001 with a typical fracture response: a) porosity and b) accumulated plastic strain ($\epsilon_p \geq 0.001$) in 2D material at* Δ *a/D* = 10

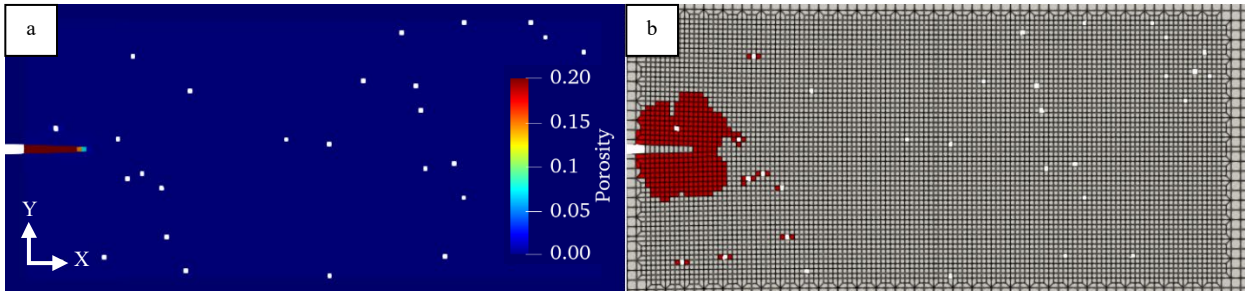

Figure 3.14. *Reference model for V_f = 0.005 with a typical fracture response: a) porosity and b) accumulated plastic strain ($\epsilon_p \geq 0.001$) in 2D material at* Δ *a/D* = 10

3.2.2. 3D Modeling

Similar to the 2D models, the presence of AM void defects in the 3D case also resulted in localized stress concentrations at the AM void defects ahead or adjacent to the current crack tip (Fig. 3.15). The 3D stress state, however, also results in 3D localized stress concentrations from AM void defects that were instantiated out-of-plane in the +Z direction (out-of-the-page in Fig. 3.15).

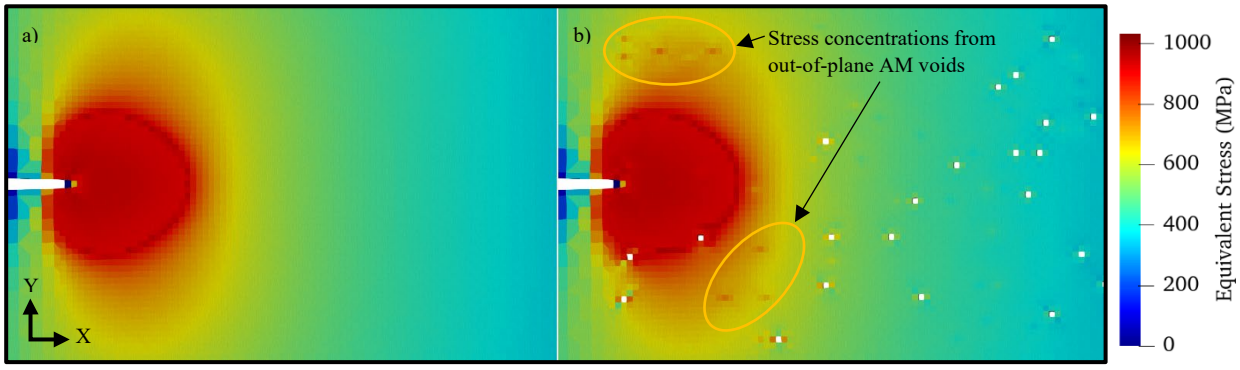

Figure 3.15. *Von mises stress fields (Equivalent Stress) in a 3D models at the constrained mid-plane (z = 0D) ahead of crack tip for a a) material without and b) with AM void defects at* $V_f = 0.005$.

The effects of increasing AM void defect volume fractions on the *R*-curves were studied for 3D models of AM Ti-6Al-4V containing: (1) isolated AM void defects that were prevented from instantiating within 2 Gurson cell thicknesses (i.e., a distance of 2*D*) of each other in any direction (Fig. 3.16) which prevented the coalescence of multiple AM voids together prior to loading, and (2) AM void defects allowed to cluster together to form a single, larger, and potentially enlongated void defect if randomly instantiated next to one another (Fig. 3.17). The former represents typical keyhole type AM defects while the latter represents lack-of-fusion AM defects (Chapter 1). Because of the stochastic nature of these AM void distributions, 50 randomly generated distributions of AM voids within the process zone were modeled for each AM void fraction, and each AM void type was studied. In general, increasing the void volume fraction resulted in higher fluctuations of the crack advance ($\Delta a/D$) for the same applied K_I loading. Outliers also increased in frequency at higher void volume fractions and especially when AM voids were allowed to

cluster as in *R*-curves for $V_f = 0.01$ (Fig. 3.17). For completeness, a perspective view of 3D crack propagation can be found in Fig. 3.18.

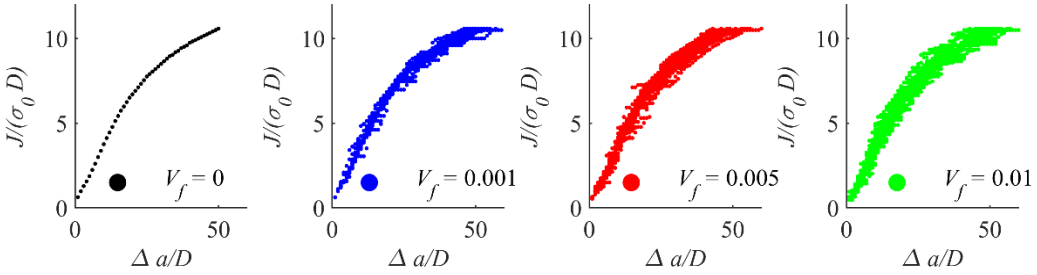

Figure 3.16. *R-curves for increasing AM void fractions, 50 samples each (AM voids separated by at least 2 D)*

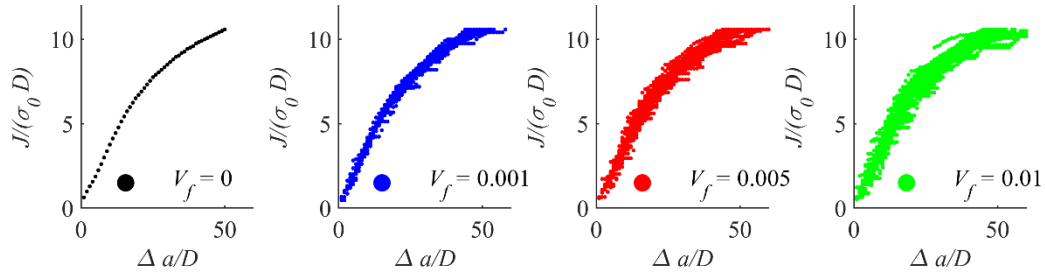

Figure 3.17. *R-curves for increasing AM void fractions, 50 samples each (AM voids permitted to cluster)*

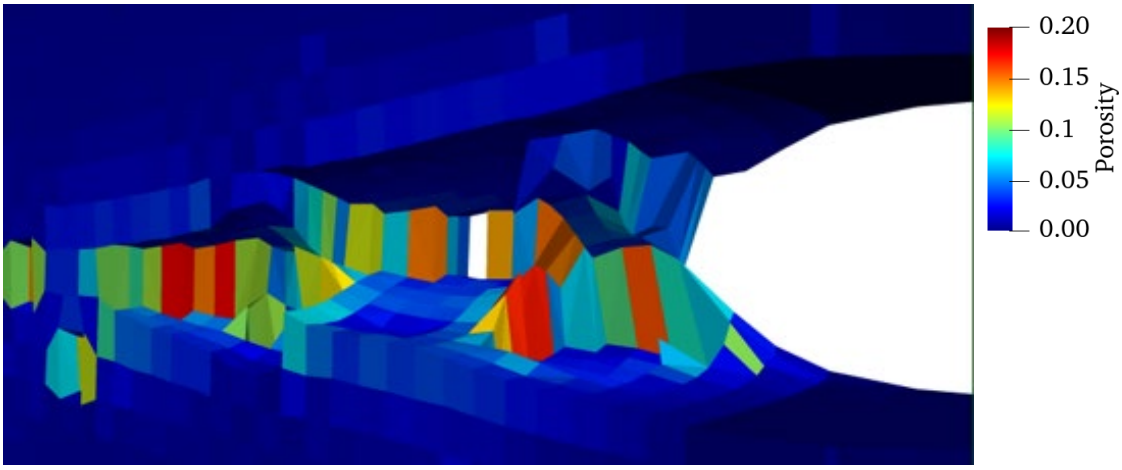

Figure 3.18. *Example perspective view of 3D crack propagation through model with $V_f = 0.01$. Gurson cells with $f \geq f_E$ have been removed from the visualization*

R-curves were formed by averaging the J-integral values at each Δa across all 50 random instantiations of 3D model structures with the same AM void fraction to generate a single average *R*-curve along with error bars denoting the standard error. The average *R*-curves for the 3D models containing isolated AM voids (Fig. 3.19) show no significant changes in the fracture toughness between a conventional versus AM Ti-6Al-4V containing AM void fractions of $V_f = 0.001$ and $V_f = 0.005$. As discussed in section 2.3, these void fractions are representative of actual AM void fractions characterized by our experiments. Higher AM void fractions of $V_f = 0.01$ and 0.02, however, resulted in a reduction in overall fracture toughness along with larger standard error. Comparing 3D models with isolated (Fig. 3.20a) versus cluster-permissive (Fig. 3.20b) AM void distributions also yielded no clear differences in *R*-curves.

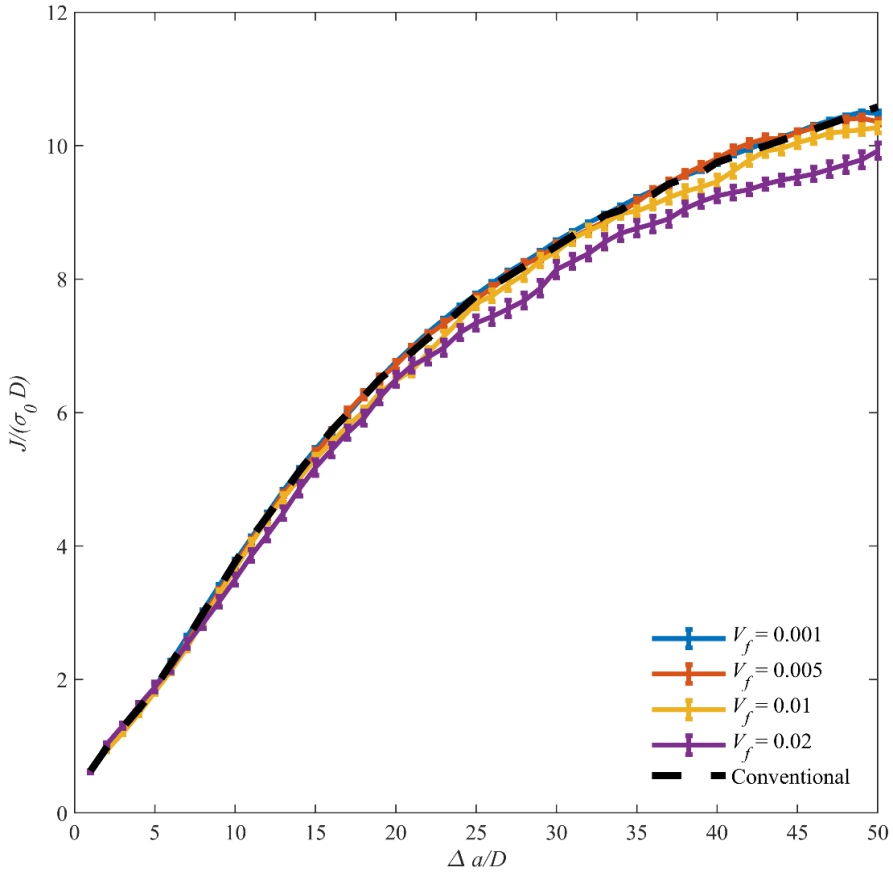

Figure 3.19. *Averaged R-curves with standard error bars (50 simulations each) for 3D analyses with increasing AM void fractions where AM voids were restricted from instantiating near one another*

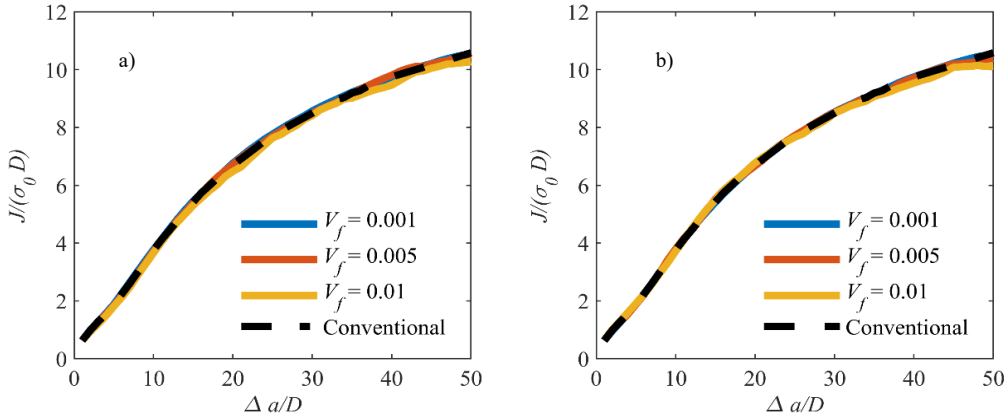

Figure 3.20. *Averaged R-curves (50 simulations) for a) AM voids restricted from instantiating near one another and b) AM voids permitted to randomly form next to one another*

The blunting and tearing moduli were determined for AM void volume fractions $V_f = 0.001$, $V_f = 0.005$, and $V_f = 0.01$, for both isolated and cluster-permissive AM void distributions from the slopes of the *R*-curves after crack initiation (1-15 $\Delta\frac{a}{D}$) and prior to reaching steady-state toughness (30-45 $\Delta\frac{a}{D}$) as shown in Fig. 3.21. The tail end of the *R*-curves were avoided due to an artifical plateau caused by approaching the programmed end of the simulation range.

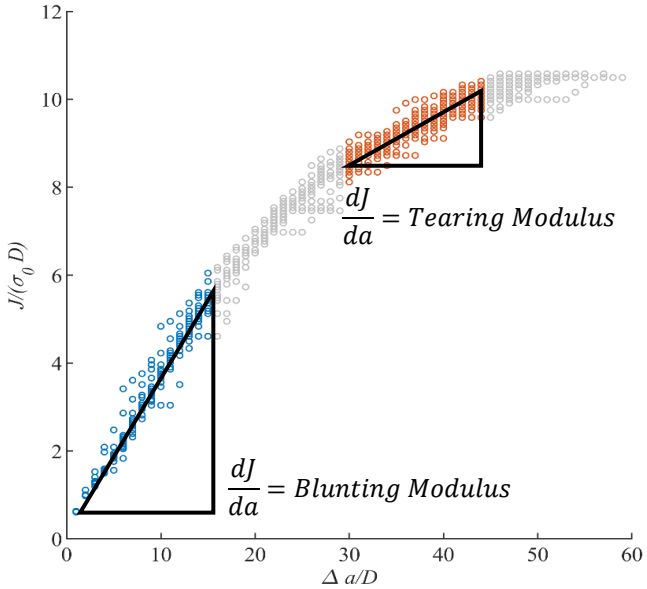

Figure 3.21. *Determining the blunting and tearing moduli*

Figure 3.22 presents the blunting and tearing moduli for AM Ti-6Al-4V normalized with respect to the blunting and tearing moduli for conventional Ti-6Al-4V without AM voids. Similar average blunting moduli were obtained across the different AM void fractions for both isolated and cluster-permissive AM void distributions. In the case of seperated AM voids, the blunting modulus only decreased very slightly (~1%) with V_f = 0.001 versus the conventional Ti-6Al-4V ($V_f = 0$). With cluster-permissive AM void distributions, the blunting modulus for the AM specimen was marginally higher than the conventional specimen, with a slight optimum (~1% increase) at V_f = 0.005. For the tearing modulus, the optimal for both isolated and cluster-permissive AM void distributions occur at $V_f = 0.005$, particularly for Ti-6Al-4V with isolated AM voids achieving over a 10% increase in the tearing modulus. Further increasing in V_f beyond 0.005, however, degrades the tearing modulus considerably.

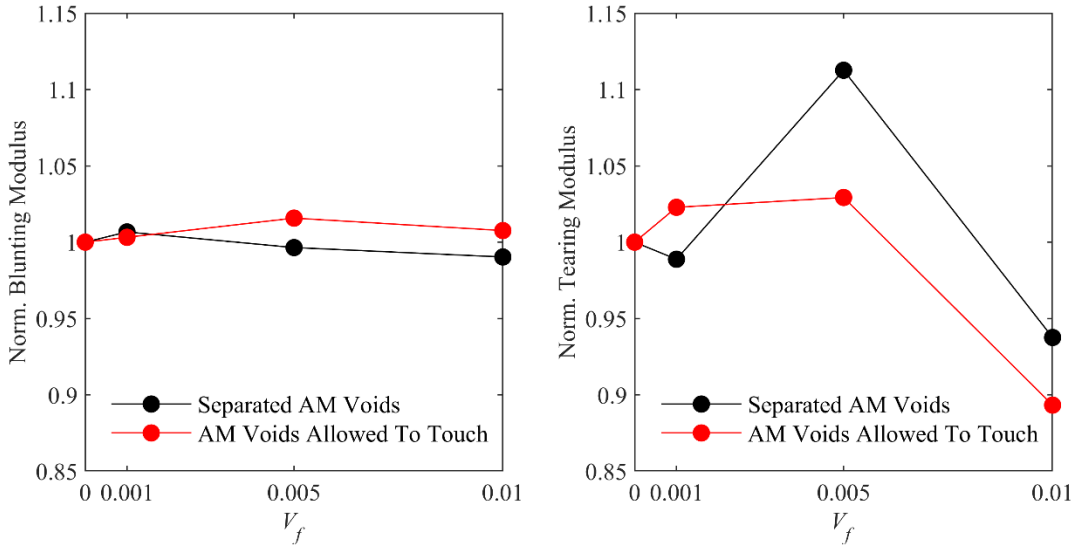

Figure 3.22. *Blunting and tearing moduli for increasing AM voids, V_f. Moduli are normalized by the modulus of a conventional material without AM void defects*

The fracture toughness at crack initation (Γ_0) was compared across increasing AM void fractions. The toughness values for materials with AM voids were again normalized by the crack initiation toughness for a conventional material without AM defects (Fig. 3.23). No significant change in crack initiation

toughness was seen in both the isolated and cluster-permissive AM void distributions. An increase in V_f generally decreases Γ_0, albeit marginally (~1% for the range of V_f considered), though a slight ~0.5% increase in Γ_0 compared with conventional metal is observed for $V_f = 0.01$ when the AM voids were allowed to cluster. The fraction of plastic work dissipated relative to the total energy applied to the AM model was also normalized with respect to that in the conventional metal and compared at crack initiation (Fig. 3.23). Both isolated and cluster-permitting AM void distributions resulted in increasing levels of plasitc dissipation with V_f at fracture initiation.

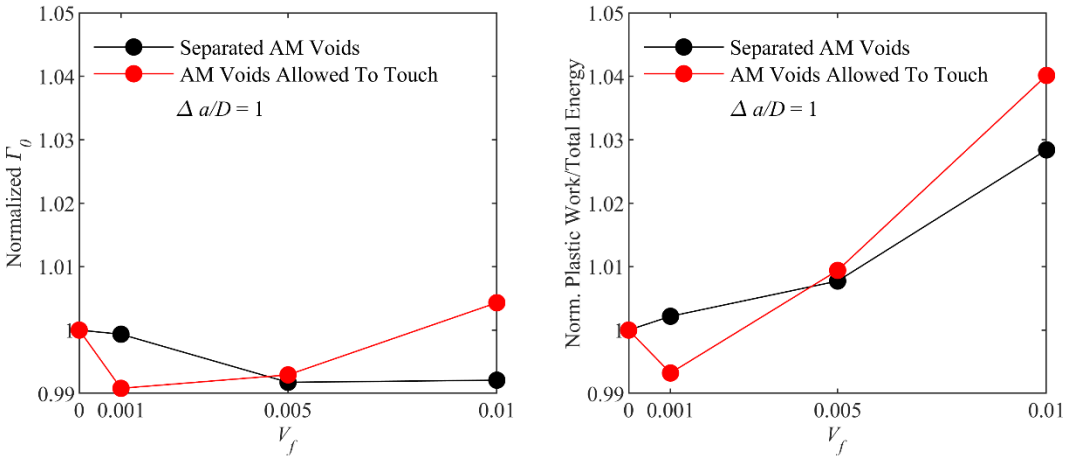

Figure 3.23. *Fracture initiation toughness (Γ_0) and plastic work/total energy for increasing V_f. Values are normalized by the modulus for a conventional material without AM voids*

3.2.3. Capturing 3D Crack-Defect Interactions: Damage Maps

The *R*-curves averaged over all 50 samples with random distributions of AM voids ultimately results in a fracture response that does not differ significantly from those of the conventional metal. However, there are specific instances where higher toughness was observed due to the strategic placement of AM voids with respect to the notch-tip or advancing crack-tip. To better visualize the damage caused by the advancing crack through a field of AM voids, *x-z* slices were taken from the 3D models parallel to the original crack plane showing the crack path and its effect on the material above and below (Fig. 3.24). The damage maps show the current Gurson cell porosity, f, overlayed on the undeformed mesh, to provide

insights into the relation between the original AM void defect location and the final damage response. Dark red denotes elements that have porosities exceding the extinction porosity ($f_E = 0.2$) indicating a complete loss of stress-carrying capacity.

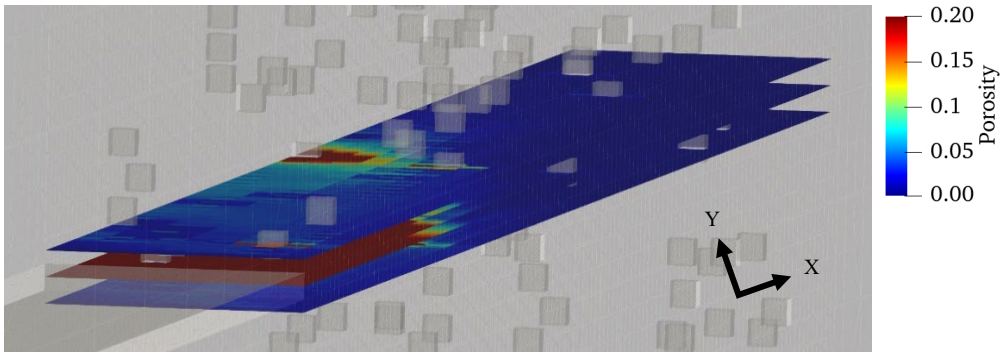

Figure 3.24. *Damage maps created from x-z slices above and below the original crack plane show material failure and porosity (void growth)*

The effects of the discrete AM void defects on the fracture resistance during early stages of monotonic fracture were investigated by relating the *R*-curves to damage associated with AM void defects located within crack extensions $\Delta a = 10D$ from the original crack tip. Two interesting material samples with cluster-permitting initial AM void distributions of $V_f = 0.01$ are studied: samples A and B (Fig. 3.25). Both of these cases exhibit repeated step jumps in fracture toughness which can exceed those in the conventional metal.

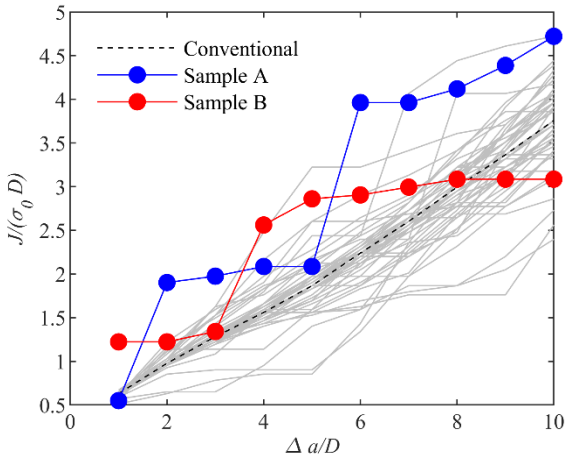

Figure 3.25. *R-curves for samples with higher toughness early in crack propagation, for* $V_f = 0.01$ *and where AM voids are allowed to touch*

Mechanisms behind these step-jumps in toughness can be traced from the damage maps of samples A and B in Fig. 3.26. The observed step jumps in $J/(\sigma_0 D)$ appear to originate from crack-blunting caused by the presence of AM void defects located within one or two D above or below the original crack planes in both samples A and B, circled in green in Fig. 3.26. This is especially evident in sample B, where the notch-tip was flanked above *and* below by two AM voids resulting in a much larger fracture initiation toughness (Fig. 3.25) and the ensuing jump in $J/(\sigma_0 D)$ at $\Delta a = 4D$. Similarly, the crack path of sample A is also flanked by AM voids above and below the propagating crack tip, but at a farther distance ahead of the notch-tip, contributing to the slower (i.e., at a larger $\Delta a/D$) step jump in $J/(\sigma_0 D)$ as seen in Fig. 3.25. Interestingly, the activiation of AM void defects away from the principal crack plane appears to promote crack tortuosity. For example, sample A experiences a second jump in $J/(\sigma_0 D)$ resulting in toughness values exceeding the other AM samples when the crack is drawn upwards and out of the original crack plane by localized damage zones eminating from the AM voids located above. Despite these toughening mechanisms, the *R*-curves of both samples appear to regress to the mean $J/(\sigma_0 D)$ after these events, once these toughening mechanisms are "evened-out" by accelerated crack growth mechanisms caused by AM voids lying directly along the crack path (e.g., AM void encircled in red in Sample B) which faciliates rapid

void coalescence and crack advancement without much crack blunting, since these AM voids are modeled to be of the same size (D) as the diameter of the propagating notch-tip.

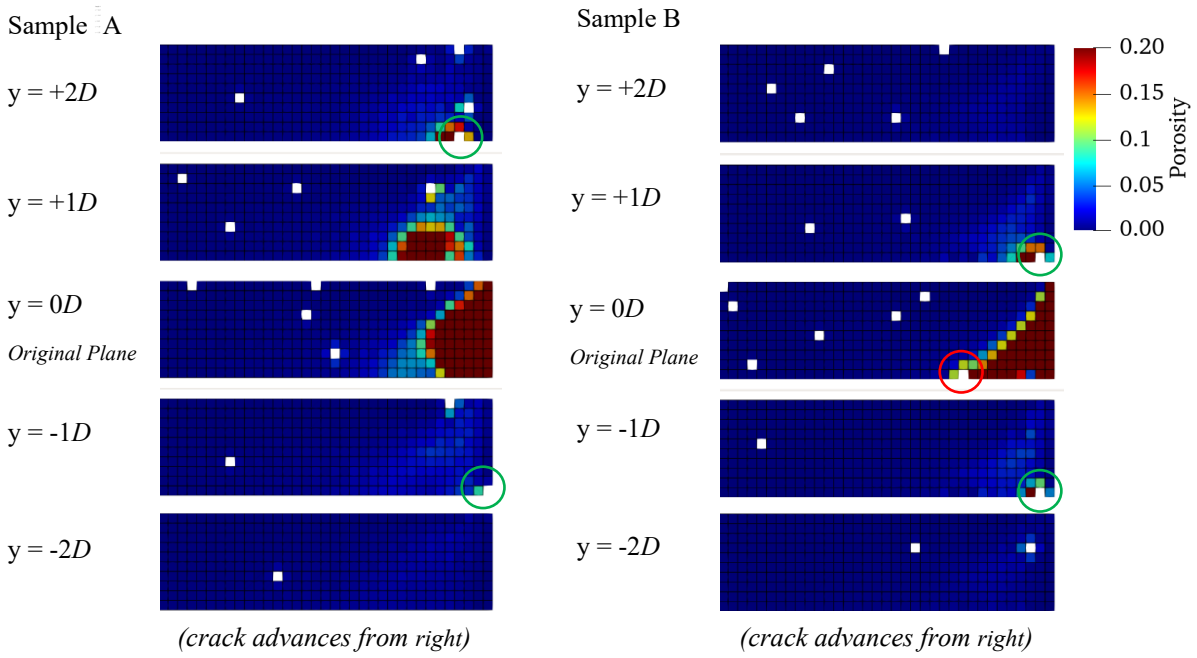

Figure 3.26. *Material failure and porosity for sample A and sample B ($V_f = 0.01$) at $\Delta a = 10D$. Locations causing blunting are circled in green, while locations circled in red may help the crack propagate*

In addition to AM void distributions that contribute to increased $J/(\sigma_0 D)$ given the same crack extension ($\Delta a/D$), there were also AM samples that exhibited lower than average fracture toughness during the early stages of monotonic fracture. Figure 3.27 highlights two such cases (samples C and D) for $V_f = 0.01$ with cluster-permitting AM void distributions. In both these underperforming samples, the initial $J/(\sigma_0 D)$ values are almost 50% lower than the average *R*-curves. Sample C, however, undergoes rapid toughening at $\Delta a = 6D$ to achieve comparable $J/(\sigma_0 D)$ to the average AM samples, while sample D continues to exhibit lower than usual $J/(\sigma_0 D)$ even beyond $\Delta a = 10D$. The damage maps in Fig. 3.28 show the presence of multiple AM voids directly on the principal crack planes of samples C and D, which facilitate rapid crack propagation at lower $J/(\sigma_0 D)$. Sample C had only 2 AM voids ahead of the crack, while sample D had twice as many AM voids directly ahead of, as well as in the neighboring planes above

and below, the initial notch-tip. The higher concentration of AM voids in sample D corresponds to the consistently lower $J/(\sigma_0 D)$, compared to Sample C which resumed its expected $J/(\sigma_0 D)$ versus $\Delta a/D$ response once the crack advances past the 2 AM voids along its path.

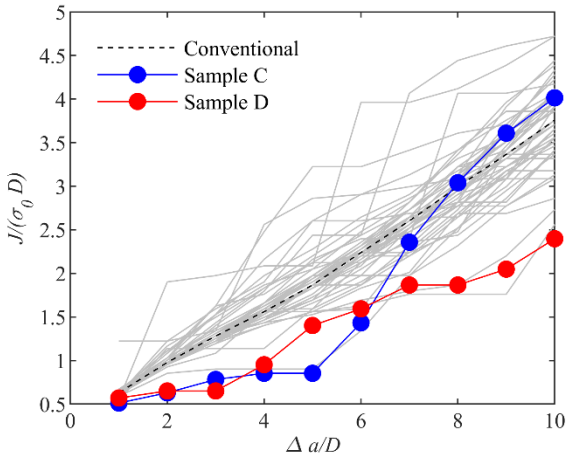

Figure 3.27. *R-curves for samples with lower toughness early in crack propagation, for $V_f = 0.01$ and where AM voids are allowed to touch*

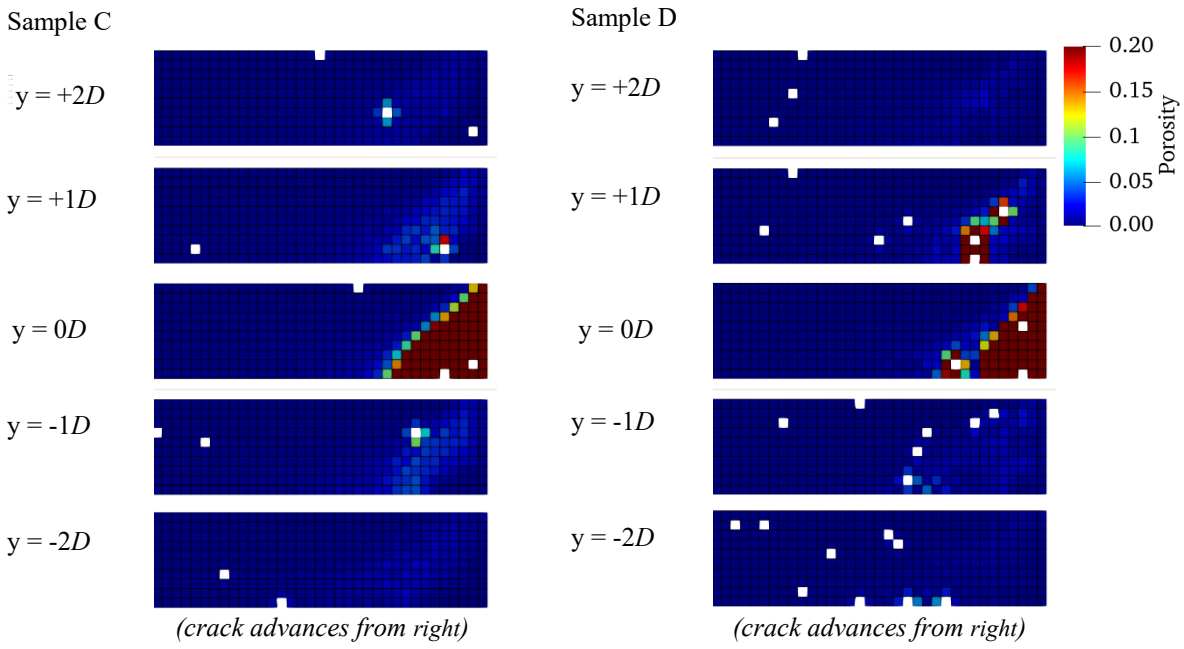

Figure 3.28. *Material failure and porosity for sample C and D at $\Delta a = 10D$. AM void defects located ahead of the crack tip on the principal crack plane appear to lower fracture toughness*

The effects of separated versus cluster-permitting AM void distributions are next examined in more detail. Fig. 3.29 highlights the *R*-curves of two material samples (samples E and F) with isolated AM void distributions which display slightly higher and slightly lower $J/(\sigma_0 D)$ relative to majority of the simulated samples within $0 \leq \Delta a \leq 10D$.

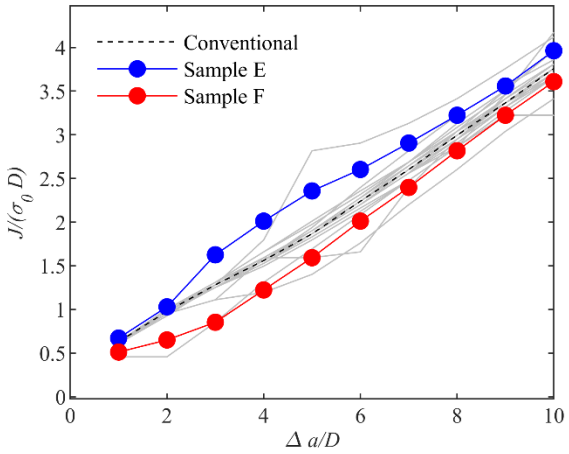

Figure 3.29. *R-curves for samples with lower toughness early in crack propagation, for $V_f = 0.001$ and AM voids allowed to touch*

Comparison of the damage maps for samples E and F in Fig. 3.30 suggests that the presence of AM voids slightly off the original crack plane (distance of 2 *D* above the crack plane for sample E) helps to blunt the crack tip and dissipate damage, while the presence of isolated AM voids directly along the crack front helps accelerate crack-growth and reduces $J/(\sigma_0 D)$. However, *R*-curves of both these samples converge to the average fracture resistance post-interaction of the crack-tip with these AM voids.

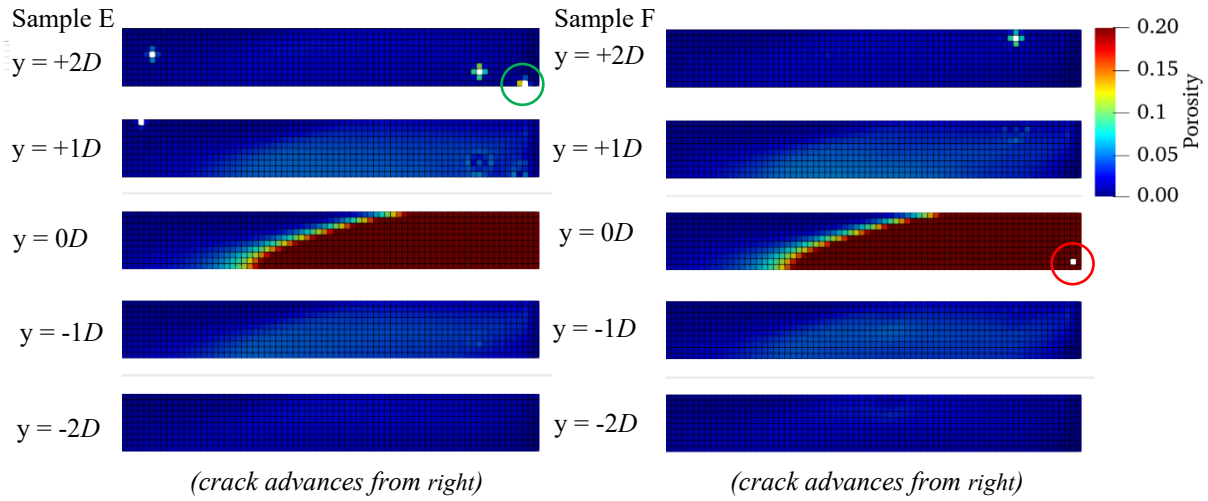

Figure 3.30. *Material failure and porosity for sample E and sample F with isolated voids at* $\Delta a = 50D$ *(*$V_f = 0.001$*, AM voids allowed to touch). Locations causing blunting are circled in green, while locations circled in red may help crack growth*

Fig. 3.31 highlights the *R*-curves for two material samples (samples G and H) displaying nominally higher fracture resistance over the entire crack propagation length of $\Delta a = 50D$, with cluster-permitting AM void distributions at $V_f = 0.01$. Of interest are the mechanisms underpinning the sharp spike in $J/(\sigma_0 D)$ at $\Delta a = 5D$ (nearly twice that for coventional Ti-6Al-4V) and the stepwise jumps in $J/(\sigma_0 D)$ beyond $\Delta a = 25D$ for Sample G, as well as the large jump in $J/(\sigma_0 D)$ near $\Delta a = 30D$ for sample H.

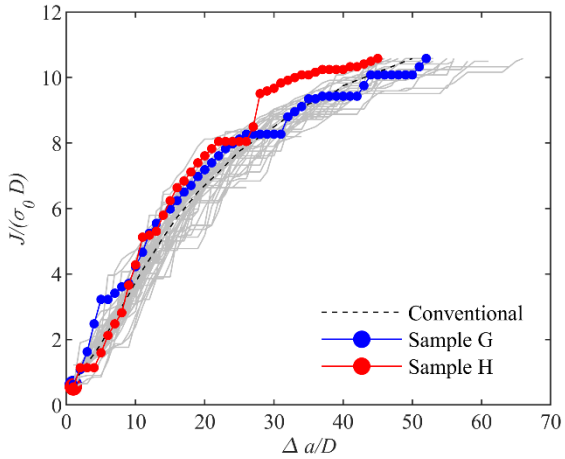

Figure 3.31. *R-curves for samples with nominally greater toughness throughout crack propagation among AM cluster-permissive materials with* $V_f = 0.01$

Both samples G and H exhibit significant crack tortousity. The crack for Sample G traverses upwards through 2 rows of Gurson cell elements almost instantaneously after initiaiton, only to reverse course and transerve downwards through 3 rows of Gurson cell elements to below the original crack plane (Fig. 3.32). This tortuous crack path appears to have been triggered by the presence of 5 clustered AM voids, 2 of which instantiated diagonal to one another at a distance +2D above the original crack plane, with an additional 2 isolated AM voids on the plane directly below (circled in green in Fig. 3.32). This cluster of AM voids steers the crack to propagate on the y = +3D crack plane. However, the presence of an additional 3 isolated AM voids on the plane below (y = +2D) accompanied by a cluster of 2 AM voids in close proximity on the y = -1D plane deviates the crack accordingly. Similarly, Sample H encounters a cluster of 6 AM voids spread across the three y = +1D to y = +3D planes early in the initial stages of crack propagation which causes the crack to propagate first along the y = +1D plane and inducing localized damage centered on the respective AM voids in the other planes. The rapid rise in fracture resistance in Fig. 3.31 coincides with the jump in the crack plane from y = 0 to y = +1D, while the tapering off of the R-curve to follow the average expected $J/(\sigma_0 D)$ versus Δa response can be attributed to the AM voids located along or neighboring to the current crack plane (y = +1D) which coalesce with the propagating crack front. As also seen in Sample G, the sharp vertical jumps in toughness correspond to switching of the preferred crack planes caused by the presence of AM voids in the neighboring ($\pm 2D$) planes. While crack growth was mostly contiguous, material failure surrounding the AM void clusters in sample G also formed small damage zones ahead of the crack prior to coalescing with the main crack (Figs. 3.33-3.34).

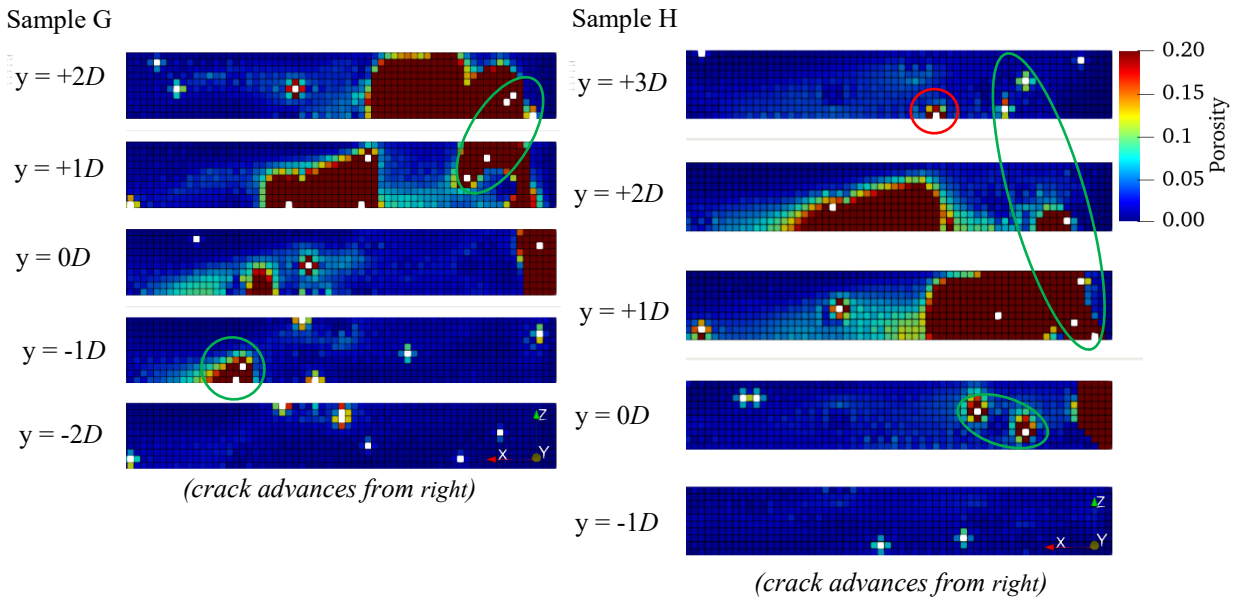

Figure 3.32. *Material failure and porosity of AM cluster-permissive samples G and H at $\Delta a = 50D$ and $\Delta a = 45D$ respectively with void fraction $V_f = 0.01$*

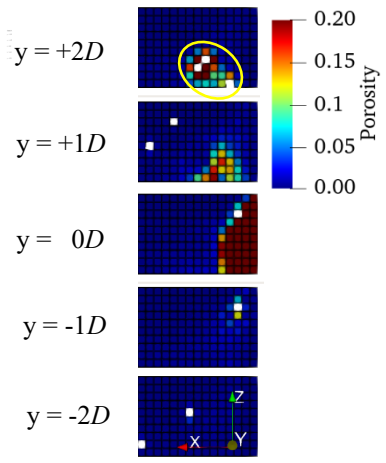

Figure 3.33. *Material failure around clustered AM voids just prior to the onset of crack tortuosity in sample G at $\Delta a = 4D$*

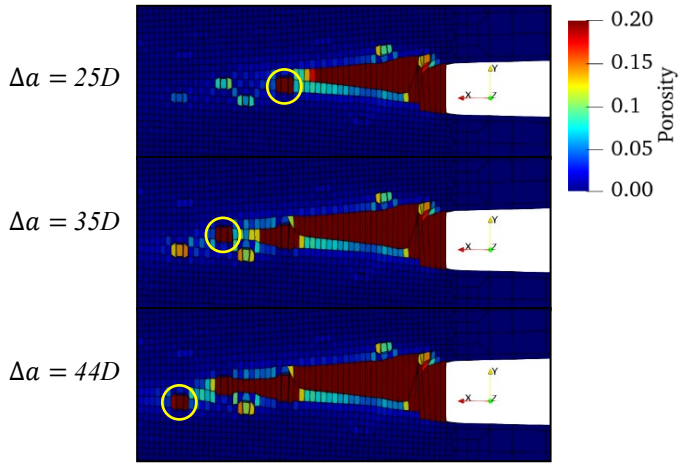

Figure 3.34. *Cross-sectional views of sample G along model midplane (z = 0) showing material failure around single AM voids prior to coalescing with main crack*

On this note, many cracks also did not develop contiguously within the AM model specimens. Some of these cracks develop from multiple damage zones formed ahead of the crack-tip and on neighboring crack planes, and coalesce together with the propagating crack-tip. To illustrate this, Fig. 3.35

highlights the *R*-curve for sample I, featuring cluster-permitting AM void distributions at $V_f = 0.005$. An unusually steep jump in $J/(\sigma_0 D)$ is observed at $\Delta a = 10D$, contributing to an *R*-curve which largely supercedes the fracture response of the other AM samples until reaching an local steady-state toughness value at the programmed simulation end.

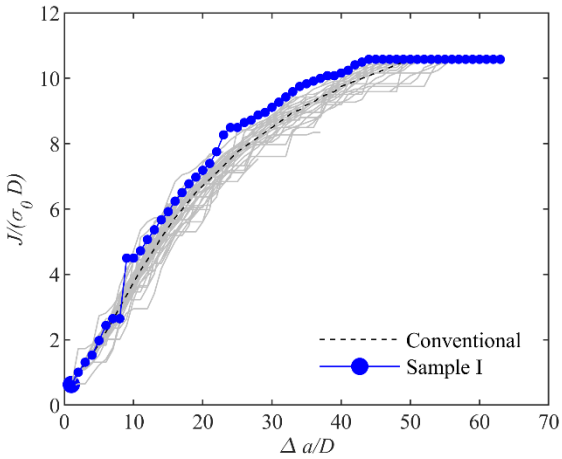

Figure 3.35. *R-curve for sample I (AM cluster-permissive instantiation with $V_f = 0.005$)*

Formation of multiple damage zones can be seen when comparing the damage maps for sample I across increaing crack advances: $\Delta a = 10D$, $\Delta a = 35D$, $\Delta a = 43D$ and $\Delta a = 63D$ (Fig. 3.36a-d). The initial toughening at $\Delta a = 10D$ is once again attributed to crack tip blunting and deviation of the propagating crack plane caused by the presence of a single AM void located at Y = +2*D,* above the original crack plane (circled in green, Fig. 3.36a). By crack advance $\Delta a = 35D$, a small isolated damge zone forms around a single AM void (circled in yellow, Fig. 3.36b), while a cluster of 3 AM voids are observed inducing a sizable damage zone a distance of nearly 30*D* ahead of the current crack tip (circled in red, Fig. 3.36b). Once again, 2 clustered AM voids on the $y = +3D$ plane appear to be responsible for deviating the main crack path, shifting it up from the $y = +1D$ plane to $y = +2$D (circled in green, Fig. 3.36b). As the K_I loading continues to increase, a bridge of 20 Gurson cells with increasing void growth can be seen joining the large clustered damage zone to the main crack, forming a growing sheet of damage dissipating background pores (Fig. 3.36c). As the large clustered damage zone and main crack grow toward each other,

the R-curve consistently remains higher than average. As the main crack reaches $\Delta a = 43D$, the large clustered AM damge zone and main crack begin to rapidly coalese (Fig. 3.36d). Therefore, the crack appears to propagate very quickly between $\Delta a = 43D$ *and* $\Delta a = 63D$, manifesting itself as a plateau in the R-curve as the cracks unite.

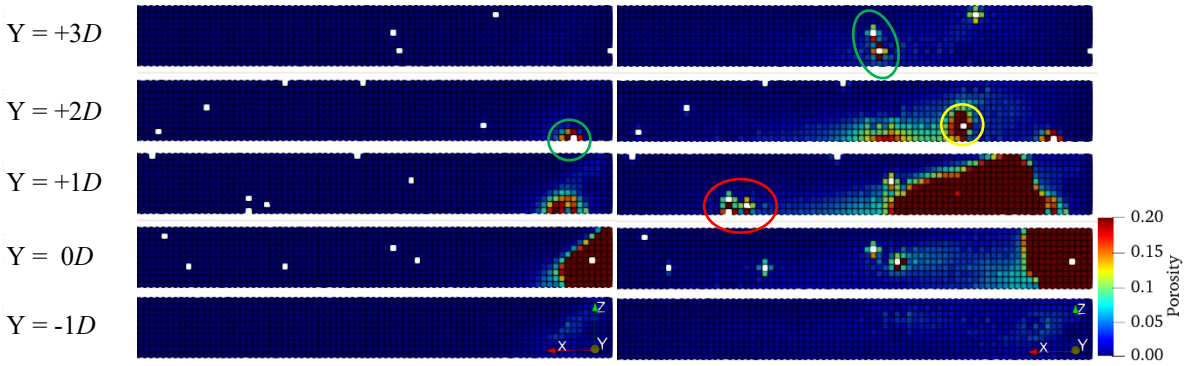

Figure 3.36a. *Material failure and porosity in sample I at* $\Delta a = 10D$

Figure 3.36b. *Material failure and porosity in sample I at* $\Delta a = 35D$

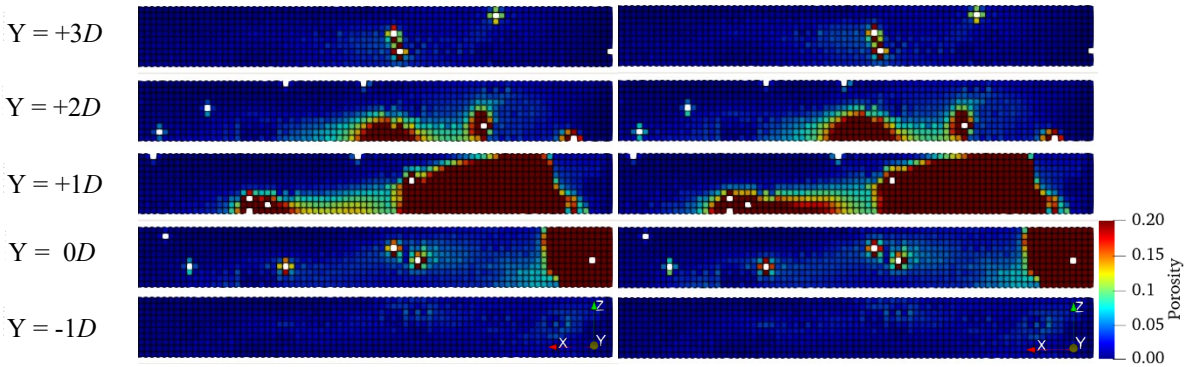

Figure 3.36c. *Material failure and porosity in sample I at* $\Delta a = 43D$

Figure 3.36d. *Material failure and porosity in sample I at* $\Delta a = 63D$

Finally, AM samples consisently underperforming the fracture resistance of conventional Ti-6Al-4V were commonly observed to have various AM voids on the same current crack plane, such as for samples J and K with cluster-permitting AM void distributions of $V_f = 0.01$ (Fig. 3.37-3.38).

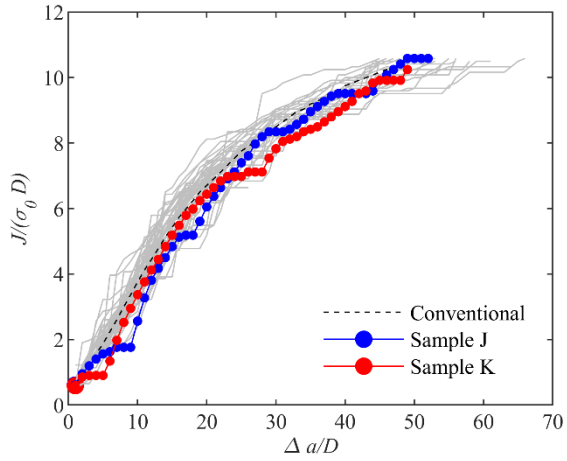

Figure 3.37. *R-curves for samples J and K with lower toughness throughout crack propagation, $V_f = 0.01$, and cluster-permissive AM void distributions*

Damage maps for samples J and K both show preferential crack propagation through planes with high density of AM void defects throughout the thickness (Fig. 3.38). The presence of AM voids on alterantive Y planes continue to induce crack deviation, but any toughening resulting from this is negated by the accelerated coalescence with clusters of AM voids on the current crack plane.

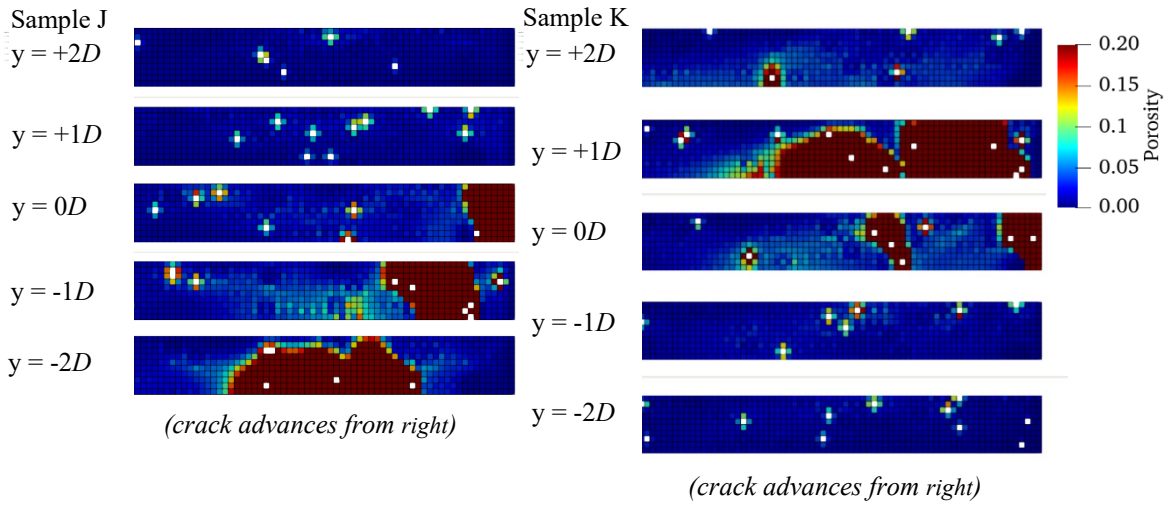

Figure 3.38. *Material failure and porosity for sample J and sample K at $\Delta a = 50D$ showing cracking along planes with relatively high AM void density*

3.2.4. *T*-Stresses in 2D Modeling

In past studies the *T*-stress has been seen to significantly influence fracture toughness in ductile materials by influencing the magnitude of triaxiality developed ahead of the crack front (Tvergaard & Hutchinson, 1994; Xia & Shih, 1995; Xia & Shih, 1996). Here the effect of *T*-stress on the fracture process was investigated by applying both positive and negative *T*-stress up to $0.5\sigma_0$ (yield strength) to a conventional Ti-6Al-4V material without AM voids using the same MBL model. *T*-stress was applied initially as a residual stress to 2D models and caused significant changes to both the size and shape of the plastic zone as shown in Fig.3.39 and as previously seen in Xia & Shih (1995).

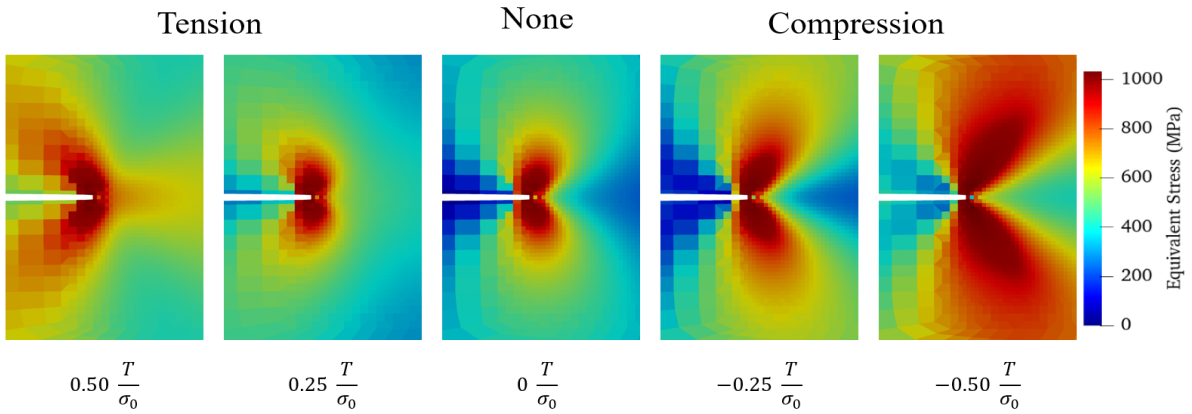

Figure 3.39. *T-stresses affecting the plane strain plastic zone at a semi-infinite crack tip, where T is the T-stress applied and σ_0 is the material yield strength*

Figure 3.40 shows the *R*-curves for conventional metals (without AM voids) under combined mode I loading with varying *T*-stress under plane strain conditions. As seen in the literature (Xia & Shih, 1995), the present results show that an increasingly positive *T*-stress generally reduces the fracture resistance, while an increasingly negative *T*-stress increases the fracture resistance. This trend is reversed however, when the same analysis is conducted under plane stress conditions (Fig. 3.41). Under plane stress conditions, the fracture resistance is significantly increased with increasing positive *T*-stress, and generally decreases with increasingly negative *T*-stress.

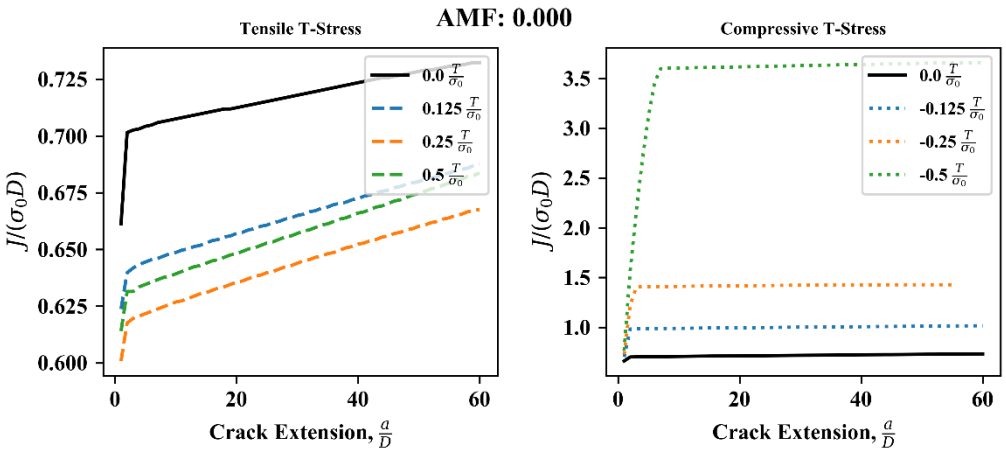

Figure 3.40. *R-curves for varying* $\frac{T}{\sigma_0}$ *in 2D conventional Ti-6Al-4V plane strain models*

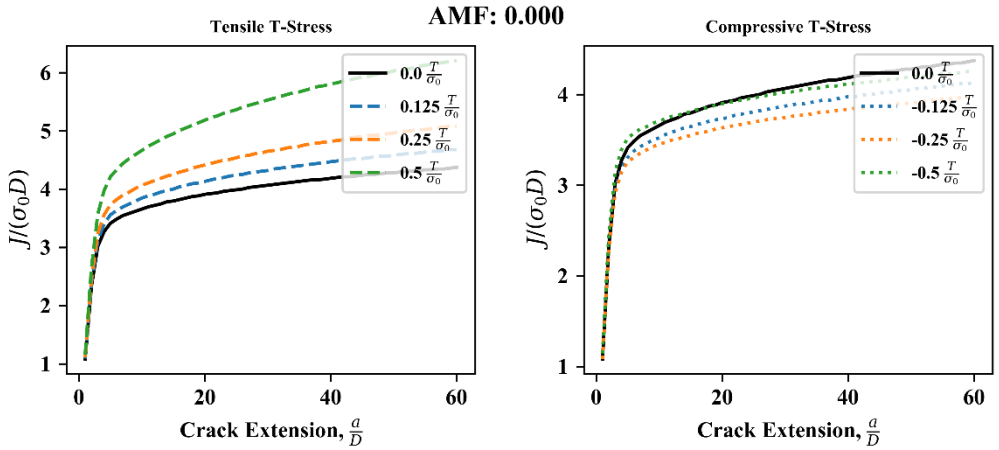

Figure 3.41. *R-curves for varying* $\frac{T}{\sigma_0}$ *in 2D conventional Ti-6Al-4V plane stress models*

3.2.5. *T*-Stresses in 3D Modeling

Of interest is the 3D fracture response with *T*-stress, also captured through *R*-curves for 3D models of conventional Ti-6Al-4V (Fig. 3.42). Just as in the 2D model under plane stress, toughness increased with increasing positive *T*-stress. However, no trend is clear trend for negative *T*-stress.

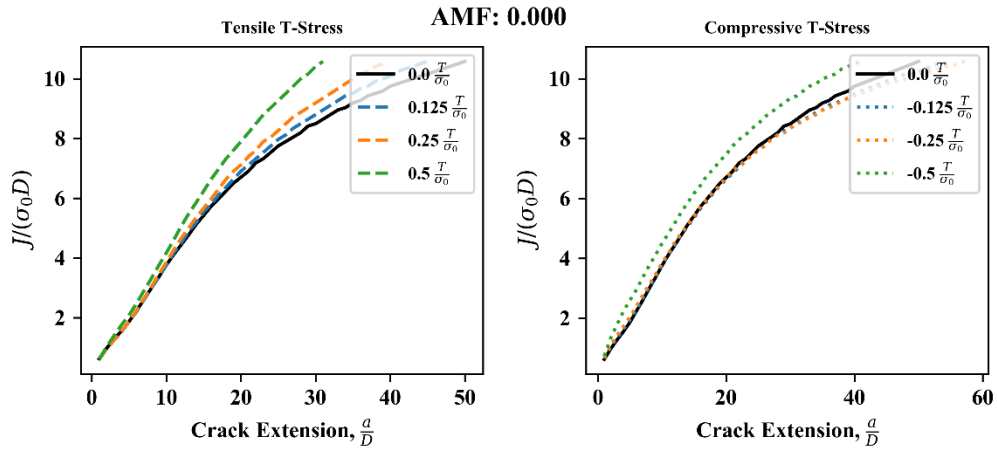

Figure 3.42. *R-curves for varying* $\frac{T}{\sigma_0}$ *in 3D conventional Ti-6Al-4V plane stress models*

More interestingly, *T*-stress appears to affect the crack path in AM materials. The same AM void cluster-permissive material sample with AM voids at $V_f = 0.01$ was subjected to 0.125 $\frac{T}{\sigma_0}$ positive and negative *T*-stress (Fig. 3.43) and experienced an altered crack path (*z = 0D*). Future work must be performed to better explore these concepts.

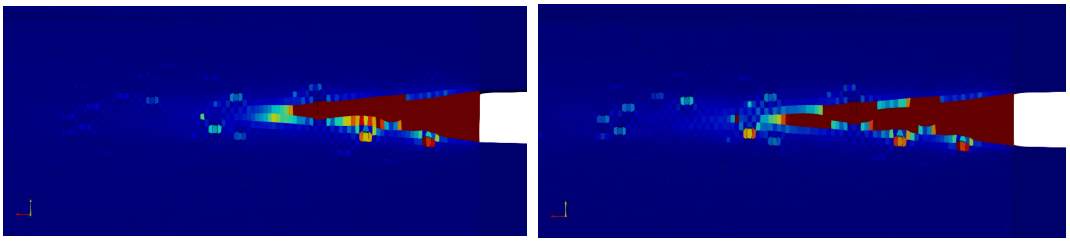

Figure 3.43. *Cross-sectional view of model midplane (z = 0D) with crack path changing between 0.125* $\frac{T}{\sigma_0}$ *positive (left) and negative (right) applied T-stress*

CHAPTER 4 – DISCUSSION AND FUTURE WORK

4.1. Limitations of the Numerical Approach

The goal of this thesis is to better understand the fracture processes in AM Ti-6Al-4V by modeling the interactions between a propagating crack front and the void defects created by un-sintered powder particles or gas entrapment bubbles during the DMLM additive manufacturing process. Some limitations of this modeling approach are discussed below.

4.1.1. AM Void Defect Representation

A simplification of the typically spherical AM void defects was made to decrease computational effort. Unlike the background voids which were modeled using computational cell elements of dimensions $D \times D \times D$ governed by the Gurson yield function, each AM void was explicitly modeled by removing the corresponding cell element. This simplification introduced two irregularities in our finite element modeling: (a) the representation of a spherical void with a cubic void, and (b) the absence of mesh refinement surrounding this cubic void which could lead to inaccuracies in predictions of quantities at the length scale of the void. The effects of both these irregularities were investigated in the unit cell studies detailed in Chapter 2. Under uniaxial tension conditions, the cubic void representation behaved very similarly to the spherical void representation, with nearly identical relationships between void volume fraction, applied strain, and uniaxial stress (Figs. 2.12-2.14). However, differences between the cubic and spherical void cell models arose under uniaxial strain loading, where a triaxial stress state was generated by the constrained lateral surfaces of the cell model. This is evident in the uniaxial stress-strain response under uniaxial straining bounds, where the unit cell with the cubic void displayed a smaller cavitation stress and underwent softening at a slower rate compared to its spherical counterpart (Fig. 2.13). This disparity in the uniaxial stress-strain response is especially apparent at higher initial void volume fractions. Additionally, the unit cell with cubic voids was consistently subjected to lower stress triaxiality compared to the unit cell with spherical voids under uniaxial straining (Fig. 2.15). Stress triaxiality appeared to plateau in the cubic void

representation past an initial volume fraction of $V_f = 0.05$, unlike unit cells with spherical voids. This decreased stress triaxiality surrounding large cubic voids may result in an underprediction in the damage extent of the surrounding Gurson cells representing the background voids in the FPZ. The unit cell studies further reveal that the simplification assumptions of using discrete cubic rather than spherical voids are reasonably accurate for AM void volume fractions not exceeding $V_f = 0.05$. Given the typical AM void fractions of $0.001 \leq V_f \leq 0.01$, this modeling assumption of cubic rather than spherical voids is likely valid for simulating crack growth and damage in an AM metal.

4.1.2. Modified Boundary Layer Finite Element Model

Perhaps a more severe limitation of the boundary layer model in this thesis is the limited out-of-plane thickness of the 3D model which may influence the transition from plane stress (on the free surface) to plane strain conditions (at the mid-plane) as seen in Fig. 4.1 (Anderson, 2005). Evidence of prevailing plane stress conditions can be seen in the predicted fracture toughness, as fracture toughness is measured higher in plane stress conditions (thin plate) and decreases with increasing specimen thickness until a plateau is reached and plane strain conditions (thick plate) are met as seen in Fig. 4.2 (Lambros, 2019).

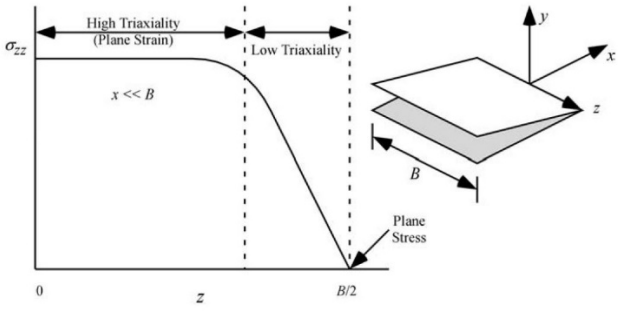

Figure 4.1. *Triaxiality versus specimen thickness (Anderson, 2005)*

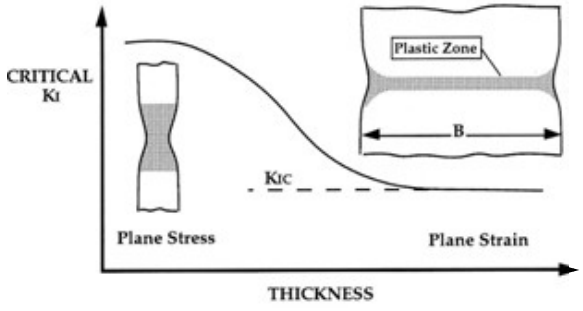

Figure 4.2. *Effect of specimen thickness on K_I toughness (Lambros, 2019)*

In this study, the MBL 3D model's predicted steady-state fracture toughness for conventional Ti-6Al-4V significantly surpasses the experimentally measured toughness values, suggesting plane stress

conditions dominate throughout the thickness. Typical fracture toughness values of conventional Ti-6Al-4V range between $J/\sigma_0 D$ = 3.99 and $J/\sigma_0 D$ = 6.84, or 84 to 110 MPa$\sqrt{\text{m}}$ in beta annealed wrought Ti-6Al-4V (Becker et al., 2015; *Titanium Alloys - Ti-6Al-4V Grade 5*, 2002; Van Hooreweder et al., 2012). Generated *R*-curves for 3D models predict fracture initiation toughness for conventional Ti-6Al-4V at roughly 0.63 $J/\sigma_0 D$, or 31.8 MPa-m$^{1/2}$ (Fig. 3.3) and a steady-state fracture toughness at roughly 11 $J/\sigma_0 D$ or 133 MPa-m$^{1/2}$ (Fig. 3.19), using plane stress assumptions in Eq. 3.1 and assuming D = 16 μm. *R*-curves for 2D models under plane strain constraints also predict fracture initiation toughness near 0.66 $J/\sigma_0 D$, or 34.2 MPa-m$^{1/2}$ (Fig. 3.3), while 2D plane strain modeling predicts a steady state toughness much lower than 3D models, at just 0.76 $J/\sigma_0 D$, or 36.7 MPa-m$^{1/2}$ (Fig. 3.9).

Ultimately, the plane strain 2D model underpredicts the fracture resistance of conventional Ti-6Al-4V, while the 3D model tends to overpredict the fracture resistance. It reasons that extending the model thickness of the 3D MBL model can help reach plane strain conditions. Following ASTM-E399 (1997) as a reference, plane strain conditions generally prevail when

$$B \geq 2.5 \left(\frac{K_{IC}}{\sigma_0}\right)^2 \tag{4.1}$$

where B is the model thickness, K_{IC} is the fracture toughness of the material, and σ_0 is the material yield stress. Assuming a typical fracture toughness for wrought Ti-6Al-4V ($K_{IC} = 80$ MPa$\sqrt{\text{m}}$) and yield stress ($\sigma_0 = 940$ MPa), the required thickness by Eq. 4.1 is 18.1 mm. The MBL model was designed with a width of 10 D, or a 10 Gurson cell thickness, to maintain a small computational and temporal expense. A large part of this modeling difficulty stems from the presence of an intrinsic length-scale in the Gurson model, D, which physically represents the spacing between the background voids. In this thesis, D = 16 μm is also representative of the AM void size. To achieve the ASTM-suggested out-of-plane thickness for plane strain conditions thus requires modeling 1,131 Gurson cells through the thickness, which is over 100× the current 3D model thickness and would significantly increase the computational expense.

The frequencies of AM void defects and background porosity in this study were selected to represent highly dense AM Ti-6Al-4V samples previously tested experimentally in the work of VanSickle et al., (2020). The optical micrographs used to measure the diameters and frequency of the AM void defects provided one method for determining a relevant range of AM void defect volume fractions (V_f). Other methods are available, including x-ray tomography and Archimedes' principle for higher porosities, and may provide a better estimate of AM void defects in AM Ti-6Al-4V. This study determined the volume fraction of AM void defects in the AM Ti-6Al-4V tensile samples to be $V_f = 0.0002$. Most highly dense AM builds today achieve a total effective porosity near $V_f = 0.005$ (*Get the Facts On… Porosity in Metal Additive Manufacturing | GE Additive*, 2021). However, high density AM builds are only achievable under ideal conditions and in bulk geometries. Due to insufficient heat dissipation by the surrounding power bed, difficulty in bridging gaps, and significant distortion when creating overhangs, complex and thin part geometries exhibit increased AM void defects (Wu et al., 2020). When using suboptimal Additive manufacturing process parameters, AM defects frequently occur just beneath the surface and along the edges of builds (subcontour defects) due to the reduced thermal conductivity of the surrounding powder bed (Fig. 4.3). Excessive energy deposition during the Additive manufacturing process can also result in keyhole defects, where the material is vaporized through multiple deposited layers, resulting in trapped gas bubbles (Panwisawas et al., 2017). Exploring crack defect interactions with higher defect concentrations near the specimen surface to account for the influence and role of surface defects as fracture initiation sites may be a subject of future work.

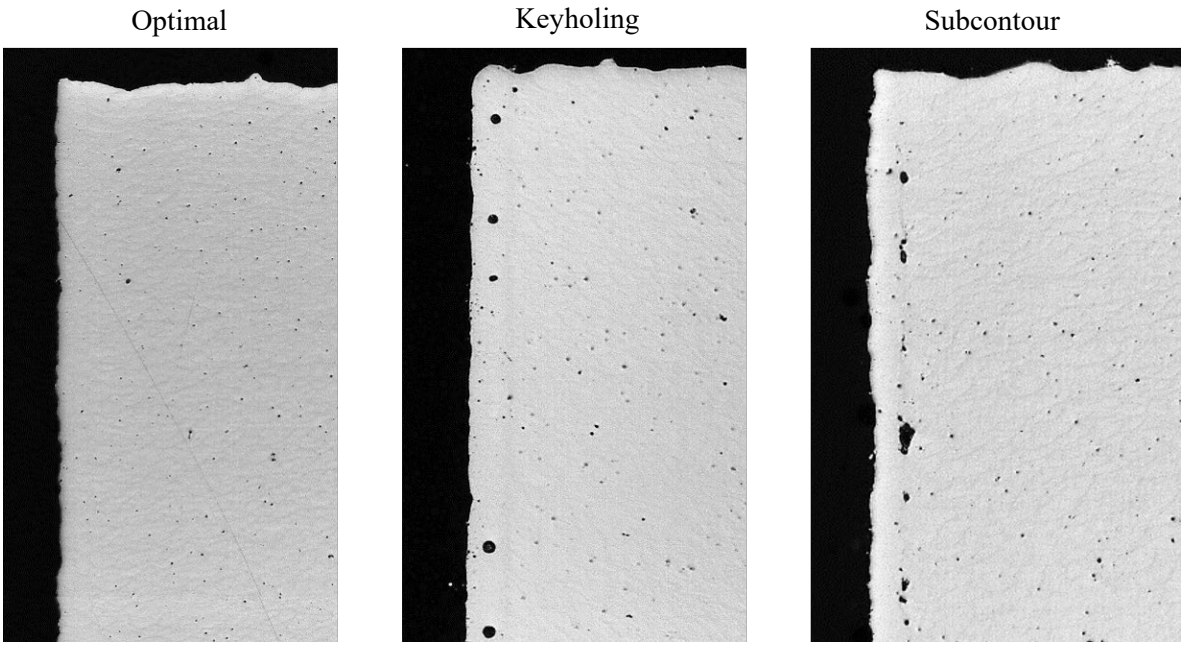

Figure 4.3. *Examples of AM builds manufactured with or without the optimal process parameters and the resulting keyhole and subcontour defects (Get the Facts On… Porosity in Metal Additive Manufacturing | GE Additive, 2021)*

The applicability of 2D models is questionable as fracture is inherently a 3D phenomenon. Unlike 2D fracture models, 3D models are able to account for the effects of stress/strain gradients and stress concentrations originating from AM voids instantiating throughout the thickness of the material (Fig. 3.15). The quantitative contributions of AM void defects and the associated damage distributions during crack growth can only be captured in 3D models, which better explain the real-world fracture processes in AM Ti-6Al-4V than 2D models. This is evident in the *R*-curves for both materials with and without AM void defects, where 2D models displayed a more brittle response (Fig. 3.9), while 3D models captured the typical rising *R*-curves seen in elastoplastic fracture mechanics associated with microvoid coalescence (Fig. 3.19). This is in part because the latter accounts for out-of-plane tearing arising from an accelerated crack extension under plane strain conditions and a delayed crack extension under plane stress conditions.

4.2. Influence of AM Void Defects

This investigation suggests the primary factors governing the crack-tip fracture resistance in AM Ti-6Al-4V are the locations of AM void defects and deflect clusters with respect to the current crack-tip. Increasing the volume fraction of AM void defects in a material alone fails to drastically affect the overall fracture response as seen in the averaged *R*-curves for the 3D finite element models (Figs. 3.19-20). While the presence of randomly instantiated and isolated AM voids can momentarily increase or decrease the local toughness, material toughness gradually tapers towards the mean value once the crack propagates past the AM void defects and defect clusters into a region relatively free of AM defects. This is especially apparent for AM materials with low void fractions, such as $V_f = 0.001$ (Figures 3.29-30). However, certain AM void defect distributions can induce prolonged periods of significantly higher or lower material toughness either at crack initiation, during crack propagation, or both, suggesting a possibility to control the toughness response by strategic placement of AM defects throughout the material.

4.2.1. Fracture Initiation

Thesis research demonstrates that the presence of AM voids near the initial notch-tip can lead to crack tip blunting, larger plastic wakes, and greater dissipation of plastic work which results in a higher fracture initiation toughness. Results show that crack tip blunting occurs when AM void defects are located just above or below the notch-tip during fracture initiation and early crack growth. In 2D models, 3 random instantiations of AM voids exhibited far greater toughness at both fracture initiation and during steady-state crack growth (Fig. 3.9). In each of these 2D models, the delay in fracture initiation can be tied to the placement of an AM void defect within one or two cell elements (*D*) from the initial notch-tip (Figs. 3.11a and 3.12a). AM void blunting was also observed in the 3D models, where AM voids that instantiated close to the initial notch-tip, but above or below the original crack plane, led to increased fracture initiation toughness (Figs. 3.25-26). In one of the 3D modeling samples, the presence of two AM voids, one directly above and another directly below the initial notch-tip, resulted in a two-fold increase in the fracture initiation toughness compared to that in the conventional metal (Figs. 3.25-26). However, AM voids lying

directly ahead of the notch-tip accelerate crack growth and reduce toughness during fracture initiation. In these simulations, AM voids have the same dimensions as the notch-tip, and thus do not contribute to significant crack-tip blunting when located directly ahead of the crack as seen in Fig. 4.4. For material samples C and D, which had cluster-permitting AM void distributions at $V_f = 0.01$, AM voids located directly ahead of the original notch-tip resulted in significantly lowered fracture toughness during fracture initiation and early crack growth (Figs. 3.27-28). Crack tip blunting and lower toughness due to AM voids directly ahead of the notch-tip can even be seen in models with single, isolated AM void defects such as material samples E and F (Fig. 3.30).

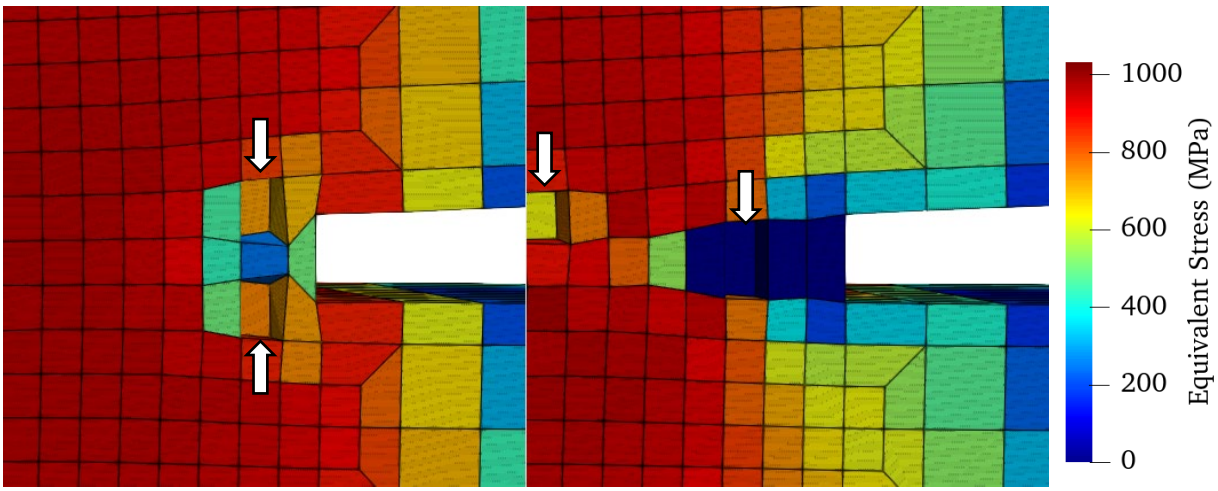

Figure 4.4. *Sample B (left), featuring reduced crack tip stress (blunted by flanking AM defects), and sample D (right), where an AM void ahead of the notch-tip facilitated crack growth, at the same applied K_I loading (arrows denote AM void defects)*

AM voids located near the crack tip also allow for greater plastic deformation and plastic work dissipation prior to the onset of fracture. In 2D models, AM voids near the crack tip generate a larger plastic wake at fracture initiation and early crack growth (Figs. 3.11b and 3.12b) compared to conventional Ti-6Al-4V (Fig. 3.10b) and the AM counterparts without AM voids near the notch-tip (Figs. 3.13b and 3.14b). Additionally, AM voids far from the notch-tip can also be seen developing plastic strain and dissipating plastic work in all AM builds (Figs. 3.11b-3.14b). In 3D models, the amount of plastic work relative to the total applied energy was calculated for each of the 50 random instantiations and averaged for each AM void

volume fraction. Increasing the number of AM void defects slightly increases the amount of plastic work dissipated relative to the total energy applied at fracture initiation by up to 4% at $V_f = 0.001$ in AM cluster-permissive models, and 3% when AM voids must form separated from one another (Fig. 3.23). It does however appear that allowing AM voids to randomly instantiate near each other increases plastic work dissipation and toughness at V_f = 0.01, while reducing it for lower V_f. Interestingly, increasing the AM void fraction had a smaller effect on the average fracture initiation toughness in the 3D models, where toughness varied by less than 1% with increasing AM void fraction (Fig. 3.23). By blunting the crack tip, creating wider plastic wakes, and dissipating more plastic work during crack initiation, crack-defect interactions in AM Ti-6Al-4V can significantly, although momentarily, increase the local material toughness. It is important to note that these phenomena may be correlated to the strain hardening exponent, as Titanium has high strain hardening. Future work may find it interesting to determine the effect of the strain hardening exponent on fracture initiation toughness though parametric studies.

4.2.2. Crack Propagation

AM void defects located above or below the crack plane ahead of a propagating crack tip may blunt the crack tip, induce crack path tortuosity, and form isolated or clustered damage zones. Thesis research demonstrates all these mechanisms contribute to the increase in fracture toughness. In a 2D model with AM void fraction $V_f = 0.001$, the presence of an isolated AM void located diagonally above the growing crack tip was demonstrated to cause a deviation in the crack path resulting in a nearly two-fold increase in local toughness from that of a conventional metal (Figs. 3.9 and 3.11). Close examination reveals that the increase in fracture resistance occurs prior to crack deviation, which suggests that the diagonal void first shields the growing crack-tip before coalescing. This ability to cause crack path deviation increases when clusters of AM voids are present. A second 2D model, with $V_f = 0.005$, shows a cluster of AM voids deviating the crack path even more significantly away from the original crack plane (Fig. 3.12). Despite the increased crack path tortuosity, this clustering of AM voids resulted in a smaller increase in fracture resistance compared that induced by the single isolated AM void (Fig. 3.9). This is potentially because of the rapid

accumulation of damage (background void growth) around this cluster of AM defects and the rapid coalescence of the damage zones with the growing crack-tip. AM void defects were also observed to increase fracture toughness through crack-tip blunting and the promotion of crack tortuosity in the 3D models. Most of the 3D models with random instantiations of AM void defects display a jagged step increase in fracture resistance oscillating about the *R*-curves of the conventional metal. Sharp increases in the fracture resistance ($J/\sigma_0 D$) often corresponded to a changing or blunted crack path, while rapid crack propagation with marginal increase in fracture resistance often corresponded to the rapid coalescence of the crack-tip with isolated damage zones directly ahead. As a case in point, Sample G, which exhibits significant crack tortuosity, features a cluster-permitting high AM void fraction of $V_f = 0.01$. The *R*-curves of Sample G were significantly higher than conventional Ti-6Al-4V up through crack extensions exceeding $\Delta a = 25D$ (Figs. 3.31-3.32). Frequent oscillations of the crack path above and below the initial crack front often coincide with close groupings of AM voids (circled in green, Fig. 3.32) and resulted in the persistent increased fracture resistance. During early crack growth, ($\Delta a = 5D$), the fracture resistance of Sample G was nearly twice that for the conventional metal because of the increase in actual crack length caused by crack tortuosity. A combination of crack-tip blunting and crack tortuosity, promoted by a single AM void defect (circled in red on Fig. 3.32), also resulted in significant increase in fracture resistance after $\Delta a = 25D$ in Sample H. Accumulated damage (background void growth) surrounding this void also suggests the contribution of crack-tip shielding and the dissipation of plastic work as contributing factors to the toughness increase. Several instances in samples G and H also show isolated damage regions developing around the AM void defects. Multiple damage zones forming above and below the original crack plane help shield the crack front, dissipate energy, and improve the local fracture toughness during stable crack propagation (Fig. 3.32).

4.2.3. AM Void Clusters

Random instantiation of AM void defects next to one another in the FE mesh results in the formation of AM void clusters. AM void clusters are found to locally increase fracture toughness by significantly curving the crack path, as seen in Sample G (Figs. 3.31-3.32) and by dissipating considerable plastic energy through the formation of multiple unconnected damage zones ahead of the crack front such as in samples G and I (Figs. 3.33-3.36). At the same time, however, the presence of AM void clusters may also be responsible for reduced fracture resistance resulting in accelerated crack growth. For example, samples J and K (Figs. 3.37-3.38) consistently exhibit lower fracture resistance compared to conventional Ti-6Al-4V. Although crack tortuosity was promoted by tight clusters of AM voids in samples J and K, it led to rapid coalescence and accelerated crack growth along planar regions with high AM void density. These results may explain why AM specimens tend to have large variations in fracture toughness responses. The formation of AM clusters may promote crack tortuosity and toughening during the initial blunting stage of crack propagation, but as the crack progresses, defect clusters can help direct the crack along the weaker fracture planes of the material. In physical AM builds, these weaker planar regions may manifest as long planar defects that often arise due to improper fusing of the powder layers, often called lack of fusion (LOF) defects (see further discussions in Snow et al. 2020).

The increased propensity for rapid crack propagation when AM voids can instantiate next to one another is also manifested in the measured tearing modulus of the 3D models. Comparisons of the tearing modulus show that when AM voids are allowed to cluster, the tearing modulus is considerably less than in AM Ti-6Al-4V with isolated AM voids (Fig. 3.22). Interestingly, the tearing modulus noticeably increases over conventional Ti-6Al-4V at void fraction $V_f = 0.005$ for all 3D models, suggesting that an optimal AM void defect fraction may exist that improves fracture toughness during later stages of crack propagation, but reduces the chance of encountering concentrated regions of AM defects. Comparisons of the blunting modulus yielded no significant change with increasing V_f (Fig. 3.22). However, as the AM void fraction increased, the blunting modulus in AM defect cluster-permitting models trended slightly higher than

conventional Ti-6Al-4V, while materials with separated AM voids had a slightly lower blunting modulus. The slightly improved blunting modulus when AM voids are allowed to cluster may be because of better crack tip blunting by the larger clusters of AM voids. Therefore, despite the increased potential of running into weaker regions densely populated with AM voids, there appears to be potential for strategic placement of clustered void defects that promote crack tortuosity and increase the local fracture toughness of AM material.

Lastly, 3D models with AM void clusters show potential for greater plastic dissipation at higher void volume fractions. In general, increasing AM void volume fractions resulted in more energy dissipated as plastic work prior to fracture initiation (Fig. 3.23). However, models permitting AM void clusters exhibited noticeably lower plastic dissipation than a conventional alloy at lower void fractions ($V_f = 0.001$) and exhibited greater plastic dissipation than alloys with isolated AM voids at higher void fractions ($V_f = 0.01$). The relatively few AM void clusters that form when $V_f = 0.001$ are likely isolated and may not be able to dissipate as much plastic work compared to the more evenly distributed damage zones created with the more dispersed AM voids that are restricted from clustering together. This effect may be negated at higher void volume fractions, where AM void clusters formed are likelier to still interact with nearby AM voids and dissipate greater plastic work.

4.3. Future Work and Material Design

In this thesis, it was shown that clusters of AM voids can create large, isolated damage zones, cause crack tortuosity, and blunt the crack tip. At the same time, planar AM void clusters resembling the elongated voids stemming from lack of fusion in the AM build are also capable of creating planes of preferential cracking and allow a crack to rapidly propagate through the material. Delineating the specific AM void placements that lead to unstable crack propagation, or significant toughening, may provide critical insights to the physical processes responsible for the variation and unpredictability in material fracture toughness in AM parts.

Future studies of interactions between cracks and AM void defects should benefit from further refining the finite element mesh within the FPZ, particularly to capture finer fatigue cracks. In the AM build, fatigue cracks have a much smaller crack tip radius and crack tip opening compared to the AM void defect diameters (Fig. 4.5) (VanSickle, 2019). Due to the AM void defect representation modeled in this thesis by deleting a single Gurson cell from the FPZ mesh, the propagating crack tip is the same width as the initial size of the isolated AM voids. The interaction between an AM void defect and a propagating crack tip may be better captured using further refined Gurson cell elements within the fracture process zone. Modeling the effects of a sharper crack (i.e., reducing the size of D) could lead to further insights into the crack-void interaction mechanics.

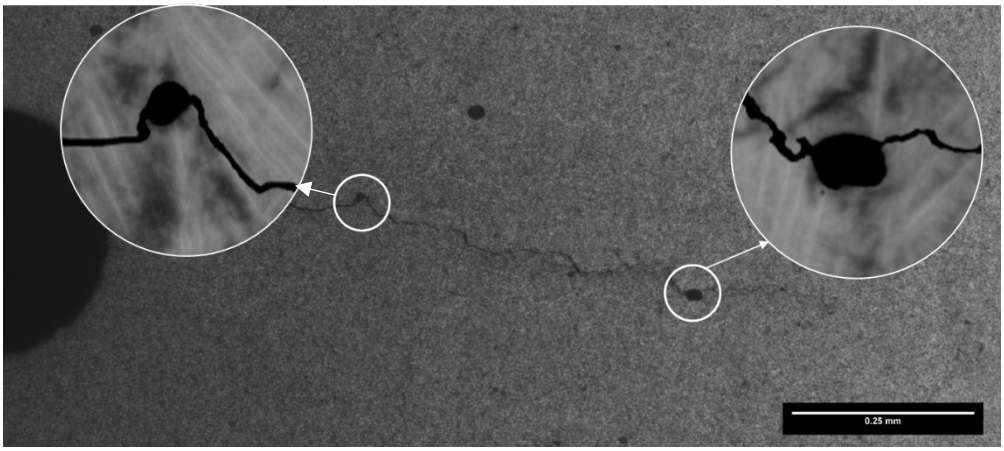

Figure 4.5. *Fatigue cracks traveling through AM defects on the surface of AM Ti-6Al-4V SEN(T)3 specimens (VanSickle, 2019)*

In this study, the fitting parameters $q_1, q_2,$ and q_3 used in the Gurson damage model were extrapolated from numerical unit cell studies to best fit the hardening exponent of the Gurson yield function (Faleskog et al., 1998), though quantitatively more accurate fracture toughness predictions can be expected by calibrating the $q_1, q_2,$ and q_3 specifically to experiments of Ti-6Al-4V. Future studies would also benefit greatly from expanding the thickness of the finite element MBL mesh beyond $10D$ as a wider model would also help increase the stress triaxiality along the mid-plane of the 3D FEM model and approach plane stain conditions (Anderson, 2005). Lastly, extending the length of the Gurson FPZ may allow for characterizing the effects of AM voids at much longer crack extensions, and could allow for the *R*-curves to reach the

steady-state toughness (Note: the applied K_I displacement fields will have to be re-centered about the current crack position).

As more is understood about the melt pool dynamics, it may be possible to design AM materials with strategically positioned AM voids to improve the fracture response of the metal. In such a scenario, the AM voids are no longer process defects, but can be considered features used to improve material performance. As demonstrated in this study, AM void defects located above or below the original crack plane can achieve increased dissipation of plastic work and lead to a more tortuous crack path. Future research can shed light into different designs that maximize an AM material's capacity for energy dissipation through void placement. Other works (Pal & Geubelle, 2014) discuss this phenomenon in granular materials, where due to stress concentrations at granule contact points, a greater fraction of impact energy can be dissipated as plastic work in granular materials in comparison to a continuum.

Fig. 4.6 demonstrates 2 potential techniques for increasing the local fracture toughness in a 2D material. Sinusoidal AM void defect placement, as first seen in Srivastava et al. (2017), promotes a winding crack path that is longer and can potentially increase the amount of energy expended. Perhaps more interesting is a field of AM voids aligned along the greatest lines of equivalent stress, as seen in Fig. 4.6b. Through the creation of stress concentrations at each AM void defect and between void clusters, there is evidence of significantly increased fracture toughness and energy dissipation in strategic AM material designs over conventional metals (Figs. 4.7-4.8).

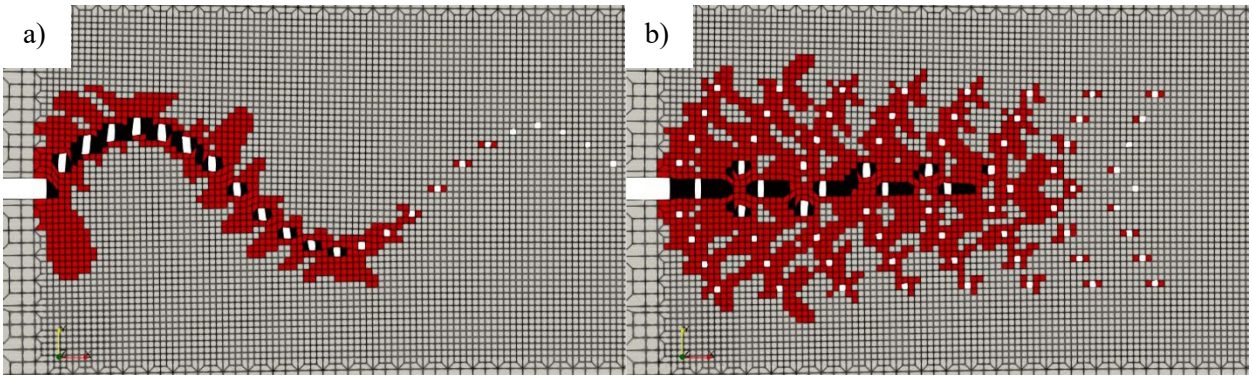

Figure 4.6. *Accumulated plastic strain ($\epsilon_p \geq 0.001$) in potential 2D material designs: a) sinusoidal void placement elongating the crack length and b) AM voids along lines of greatest stress.*

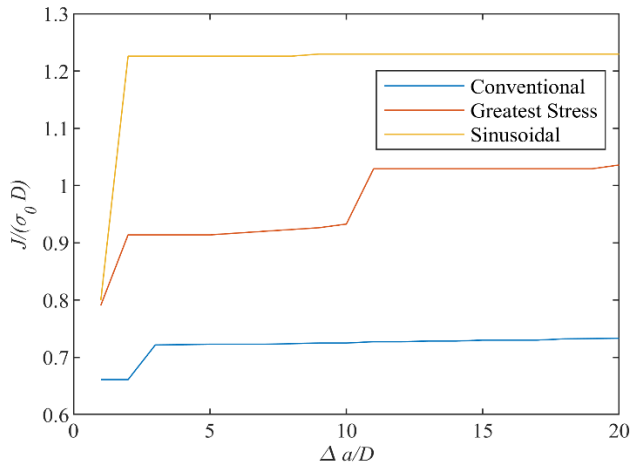

Figure 4.7. *R-curves for strategic 2D AM material designs*

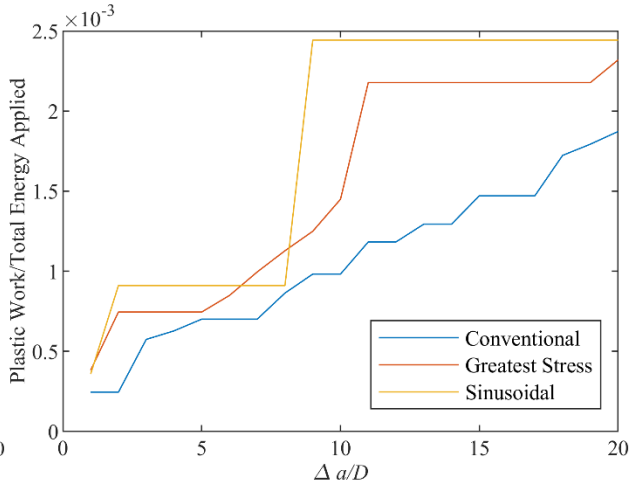

Figure 4.8. *Plastic work dissipated by strategic 2D AM material designs*

Of greater interest is the design of 3D AM materials where AM voids are placed to promote crack tip blunting, crack tortuosity, and energy dissipation. Unlike the proposed 2D material designs in Fig. 4.6 which are designed about an existing notch-tip, a more applicable design of AM void placements that may better account for an arbitrary fracture initiation site is using a repeated 3D pattern. Such a material design concept is proposed (Fig. 4.9), where AM void clusters are patterned through a 3D model with the goal to induce crack tortuosity, dissipate energy away from the crack tip, and significantly blunting the crack tip after coalescence. AM void clusters were patterned along the $x-y$ plane, creating two identical but diagonally offset sheets of AM clusters that alternate through the thickness ($z-$ direction) of the 3D model

as seen in Fig. 4.9 in black and red. Sheets of AM void clusters were kept a spacing of 1D apart (i.e., only 5 sheets of patterned AM voids were instantiated in our 10D wide 3D model, each plane separated by 1D along the thickness). AM void clusters were given an "L-shaped" geometry that may both promote energy dissipation and crack tortuosity through promoting daughter cracks, as well as create a "crack sink" by significantly blunting the crack tip with large and vertical AM voids formed by instantiating 2 single AM voids adjacently.

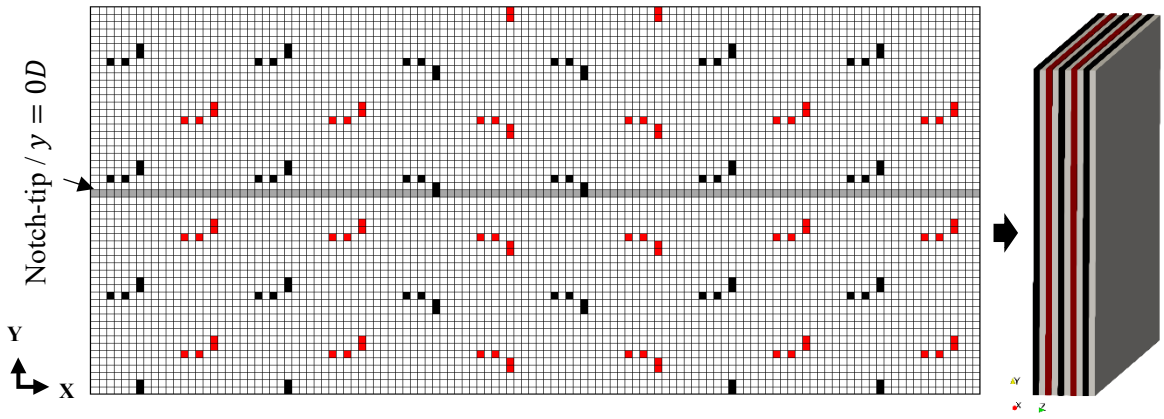

Figure 4.9. *A proposed 3D AM void pattern (left) would have shifted alternating layers shown as black and red in the oblique view (right) of distributed and diagonally aligned AM void clusters along the $z-$ direction. The gray line marks the starting crack plane ($y = 0D$)*

The design of strategic AM void configurations shows promising results and can lead to refined patterns of AM voids that significantly improve the fracture response over conventional Ti-6Al-4V throughout nearly the entire simulated K_I loading by 5-10% or more (Figs. 4.10-4.11). Design of AM void cluster geometry also shows promise in inducing considerable crack tip blunting (Fig. 4.12) and damage dissipation through void growth away from the crack tip (Fig. 4.13).

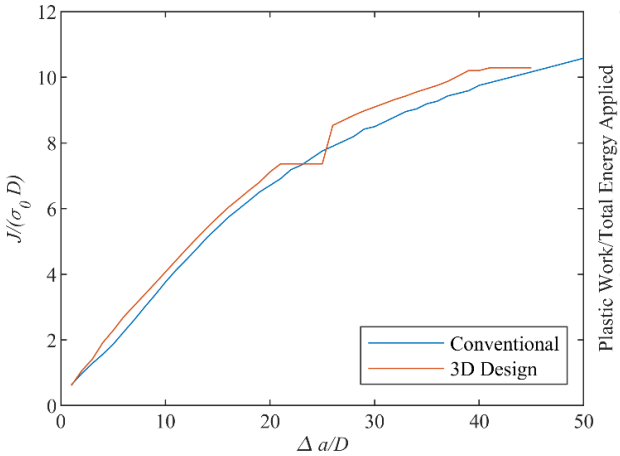

Figure 4.10. *R-curves for the proposed 3D AM material design versus conventional Ti-6Al-4V*

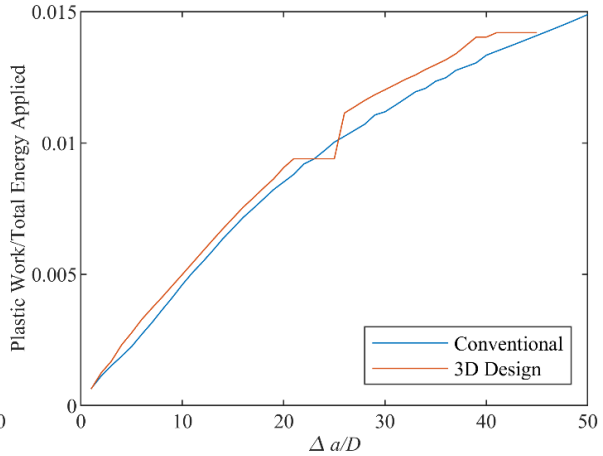

Figure 4.11. *Energy dissipated through plastic work in the proposed 3D AM material design versus conventional Ti-6Al-4V*

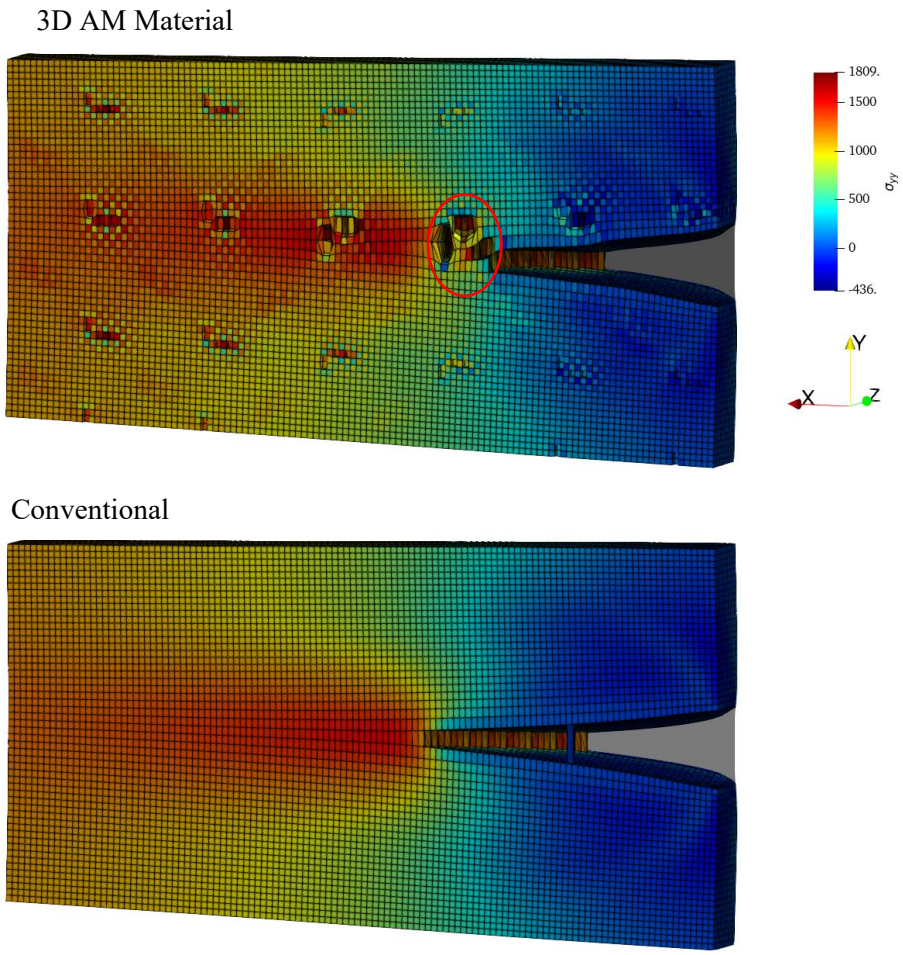

Figure 4.12. *Significant crack tip blunting in 3D models (seen by reduced σ_{yy} directly ahead of the crack tip) can result from the coalescence of a propagating crack tip with a large, vertical AM void/damage zone.*

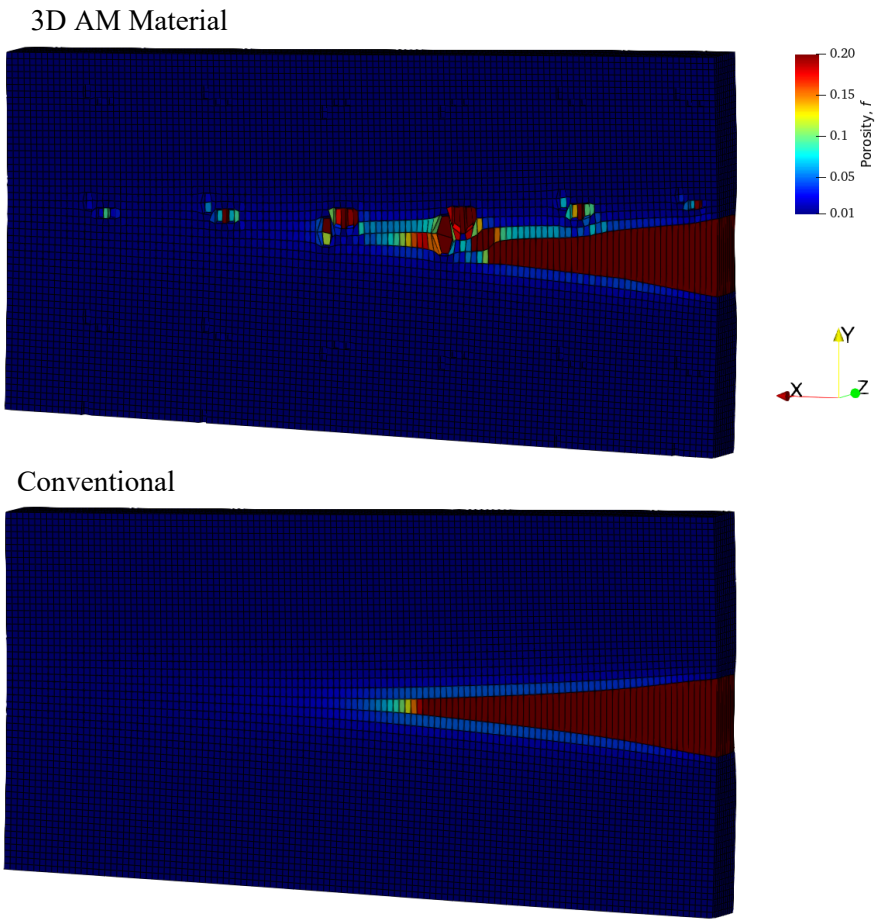

Figure 4.13. *Damage dissipation in 3D models via void growth can be seen away/ahead of the crack tip in strategically placed/designed AM void clusters*

For better insight on the performance of AM materials under real world use, the effects of *T*-stress on the fracture response as well as fatigue loadings may warrant further investigations. While this thesis briefly explores the effect of *T*-stress on crack propagation, crack path, and the perceived toughness, more work should be done to explore the role of *T*-stress on a large sample of random AM void instantiations, particularly for 3D models with increased thickness. Fatigue studies may also provide insights into the effect of cyclic loadings on the fracture response of AM materials. The AM models in this thesis have shown the potential for crack paths to deviate towards planes with dense populations of AM defects, which allow for rapid, unstable crack propagation. Future studies can provide insights into the effects of fatigue

pre-cracking on the ability for the crack to deviate along planes with lower fracture toughness, which could potentially lead to pre-mature failure of the AM specimen.

Finally, the ability to extract quantitative information rapidly from numerical simulations opens the door to the possibility of leveraging artificial intelligence to a priori determine the fracture response of an AM material. Data such as the positions of AM voids with regard to the notch-tip, the positions of AM voids and clusters in relation to their neighboring voids, the plastic work dissipated in the vicinity of each AM void, the deviation in crack paths, formation of isolated damage zones ahead of the crack front, and more, can be tabulated and fed into a machine learning algorithm for crack path predictions. Due to the black box nature of many machine learning algorithms, a supervised decision tree or random forest approach would be selected as the first candidate algorithm. Decision trees, and to a lesser extent, random forest algorithms can provide insight into the importance each physical quantity has on determining the predicted fracture toughness. However, due to the complexity required to understand the secondary and tertiary effects that AM void placement and AM void groupings may have on the crack path and overall fracture response, a deep neural network may be necessary. While it is more difficult to extract the reasoning and the physical implications behind the predictions of deep neural networks, they have the capability to learn from higher level features in the data, with less domain expertise needed and much less data preparation or feature extraction required. Although neural networks are notorious for requiring large amounts of training data, their ability to notice patterns that are not intuitive to human researchers presents a valuable asset to even seasoned researchers and may lead to a greater understanding of the variation in fracture response for AM Ti-6Al-4V builds.

CHAPTER 5 – CONCLUSIONS

The main goal of this thesis research was to explore the relationships between dual-scale porosity and crack-defect interactions in AM Ti-6Al-4V to better predict the fracture response of AM components. To accomplish this, a numerical approach in both 2D and 3D was implemented based on a small-scale yielding, modified boundary layer model with imposed monotonic K_I remote displacement loading. The intrinsic background porosity in the FPZ was modeled with multiple rows of void-containing cells governed by a Gurson yield function, while the larger AM void defects were explicitly modeled as discrete voids randomly instantiated in the FPZ finite element mesh at various volume fractions. Due to the stochastic nature of AM void defect distributions, 50 models randomly seeded with AM void defects were performed for each AM void fraction for two scenarios: one where AM voids were kept separate representing keyhole defects from gas entrapment and again where AM void defects were allowed to cluster together to form lack-of-fusion type defects.

Both the 2D and 3D numerical models developed in this thesis were able to capture the void growth, dual-scale void interaction and coalescence mechanisms. These intricate mechanisms ultimately resulted in crack path tortuosity, as well as variation in fracture resistance as seen in actual AM Ti-6Al-4V specimens. However, the applicability of the 2D model to fracture and fatigue is questionable, as it fails to account for the effects of stress/strain gradients and stress concentrations originating from AM voids instantiating throughout the thickness of an AM specimen. As a result, the 2D models tend to exhibit a much more brittle fracture response of the AM specimen compared to the 3D model predictions. However, the 3D models in this thesis are not sufficiently thick to fully-achieve plane strain conditions along the midplane, resulting in over-predictions in the fracture resistance even for conventional Ti-6Al-4V. A model 100 times thicker is expected to produce plane strain conditions at the model midplane and predict a more realistic fracture toughness. Thus, the actual fracture toughness predictions lie in between the 2D and 3D models. The simplified representation of typically spherical AM void defects as cubic voids was found to be acceptable for volume fractions below V_f = 0.05, which is well above the porosity required to model typical AM

specimens as determined from optical micrographs of AM Ti-6Al-4V specimens. Above void volume fractions of V_f = 0.005, the main difference between spherical and cubic void representations was a decreased amount of triaxial stress around cubic voids, which would decrease the model's accuracy as the Gurson model has been found to overpredict failure strain in a low triaxial stress state.

Increasing the levels of AM defects within the levels typically seen in modern Additive manufacturing processes did not significantly influence the average overall fracture response of AM models in either the 2D or 3D, even when AM voids were permitted to cluster. For higher AM void volume fractions, a graduate decrease in average crack growth resistance curves was seen in 3D models. However, although the *average* response of all 50 runs in each case is less sensitive to the AM void volume fraction, the variability in the fracture response increased with increasing levels of AM void defects in both the 2D and 3D models, particularly in high void fractions when AM voids were permitted to form clusters. Fracture resistance curves for 3D models frequently oscillated between periods of increased and reduced fracture resistance compared to conventional alloys. An optimal AM void fraction may exist as the blunting modulus was slightly improved in AM materials when AM voids were allowed to cluster, and the tearing modulus first increased with AM void levels before decreasing considerably. The effect of *T*-stress on crack-defect interactions was briefly explored in this study and warrants further investigation. Preliminary results suggest *T*-stress is capable of manipulating the location and shape of the plastic zone in 2D models and altering the preferred crack path though AM alloys in 3D models.

Damage mechanisms resulting from crack-defect interactions between AM void defects and background microvoids were identified along with their impact on the fracture resistance of AM models. During fracture initiation, the presence of AM voids near the model notch-tip leads to crack tip blunting, larger plastic crack wakes, and increased plastic dissipation. Crack tip blunting was identified as the primary energy absorption mechanism responsible for increased fracture initiation toughness. AM models with single or clustered AM voids located along the midplane directly above or below the crack notch-tip can increase fracture initiation toughness up to two-fold that of conventional alloys. AM voids near the notch-

tip during fracture initiation also increased plastic energy dissipation. Plastic wakes in 2D models were significantly larger when AM void defects were found near the notch-tip and show plasticity developing farther ahead of the crack tip during early crack growth from the development of high localized stress concentrations around each AM void defect. Generally, these toughening mechanisms are magnified when AM voids are clustered. Because the crack notch-tip width is equal to the size of a single undeformed AM defect in our model, AM voids located directly in line with the main crack path do not provide significant crack blunting effects and appear to facilitate crack propagation. Regardless if AM void defects were positioned to toughen or weaken the material, these crack-defect interactions typically gradually regress to the mean fracture resistance as the crack continues to propagate.

After early-stage crack propagation, AM void defects located above or below the crack plane ahead of a propagating crack tip also increase the fracture toughness by again blunting the crack tip, forming isolated or clustered damage zones ahead of the crack tip, and inducing crack path tortuosity. Just as during fracture initiation, AM voids flanking a propagating crack blunt the crack tip and dissipate plastic energy through significant void growth around AM voids far from the crack which are left behind in the plastic wake. AM voids clustered ahead of the crack can also create large, isolated damage zones that grow through microvoid coalescence and result in prolonged periods of crack growth where the local fracture toughness exceeds that of conventional alloys until rapid coalescence with the main crack occurs. Perhaps the most impactful crack-defect toughening mechanism identified during crack propagation is crack path deviation. Clusters of AM void defects located above or below the main crack plane tend to coalesce and with the advancing crack tip to cause significant deviations from the original crack plane. Because the tortuous crack-path is significantly longer than a planar crack path, the process results in a greater dissipation of plastic work. However, crack tortuosity can also facilitate fracture depending on the location and concentration of AM voids. Vertically stacked AM void clusters tend to cause crack-tip blunting, while horizontally stacked AM void clusters create preferential planes for rapid crack growth. Premature failure of AM Ti-6Al-4V fatigue specimens seen in prior experiments may be the result of curving crack paths that

are drawn to these weaker planes in the material. Through harnessing these crack-defect interactions of the dual-scale porosity found in AM alloys, material design using strategic void placement suggests that future AM components may purposefully include void defects to produce superior fracture resistance over conventional alloys.

REFERENCES

Anderson, T. L. (2005). *Fracture mechanics: Fundamentals and applications* (3rd ed). Taylor & Francis.

ASTM E399-90 (1997), Standard Test Method for Plane-Strain Fracture Toughness of Metallic Materials, ASTM International, West Conshohocken, PA, 1997, www.astm.org. (n.d.).

Ayachit, U. (2015). *The ParaView guide: Updated for ParaView version 4.3* (L. Avila, Ed.; Full color version). Kitware.

Becker, T. H., Beck, M., & Scheffer, C. (2015). MICROSTRUCTURE AND MECHANICAL PROPERTIES OF DIRECT METAL LASER SINTERED TI-6AL-4V. *The South African Journal of Industrial Engineering*, *26*(1), 1. https://doi.org/10.7166/26-1-1022

Casalino, G., Campanelli, S. L., Contuzzi, N., & Ludovico, A. D. (2015). Experimental investigation and statistical optimisation of the selective laser melting process of a maraging steel. *Optics & Laser Technology*, *65*, 151–158. https://doi.org/10.1016/j.optlastec.2014.07.021

Chastand, V., Quaegebeur, P., Maia, W., & Charkaluk, E. (2018). Comparative study of fatigue properties of Ti-6Al-4V specimens built by electron beam melting (EBM) and selective laser melting (SLM). *Materials Characterization*, *143*, 76–81. https://doi.org/10.1016/j.matchar.2018.03.028

Chew, H. B., Guo, T. F., & Cheng, L. (2005). Vapor pressure and residual stress effects on failure of an adhesive film. *International Journal of Solids and Structures*, *42*(16–17), 4795–4810. https://doi.org/10.1016/j.ijsolstr.2005.01.012

Chu, C. C., & Needleman, A. (1980). Void Nucleation Effects in Biaxially Stretched Sheets. *Journal of Engineering Materials and Technology*, *102*(3), 249–256. https://doi.org/10.1115/1.3224807

Clinton, R. G. (n.d.). *Deputy Manager, Science and Technology Office NASA, Marshall Space Flight Center 1!* 26.

Cui, Y., Gao, Y. F., & Chew, H. B. (2020). Two-scale porosity effects on cohesive crack growth in a ductile media. *International Journal of Solids and Structures*, *200–201*, 188–197. https://doi.org/10.1016/j.ijsolstr.2020.04.035

Dutta, B., & Froes, F. H. (2016). *Additive manufacturing of titanium alloys: State of the art, challenges and opportunities*. Butterworth-Heinemann is an imprint of Elsevier.

Faleskog, J., Gao, X., & Shih, C. F. (1998). Cell model for nonlinear fracture analysis – I. Micromechanics calibration. *International Journal of Fracture*, *89*(4), 355–373. https://doi.org/10.1023/A:1007421420901

Faleskog, J., & Shih, C. F. (1997). Micromechanics of coalescence—I. Synergistic effects of elasticity, plastic yielding and multi-size-scale voids. *Journal of the Mechanics and Physics of Solids*, *45*(1), 21–50. https://doi.org/10.1016/S0022-5096(96)00078-6

Foehring, D., Chew, H. B., & Lambros, J. (2018). Characterizing the tensile behavior of additively manufactured Ti-6Al-4V using multiscale digital image correlation. *Materials Science and Engineering: A*, *724*, 536–546. https://doi.org/10.1016/j.msea.2018.03.091

Gao, X., Faleskog, J., & Shih, C. F. (1998). Cell model for nonlinear fracture analysis – II. Fracture-process calibration and verification. *International Journal of Fracture*, *89*(4), 375–398. https://doi.org/10.1023/A:1007410825313

Get the Facts on… Porosity in Metal Additive Manufacturing | GE Additive. (2021, March 10). https://www.ge.com/additive/blog/get-facts-porosity-metal-additive-manufacturing

Gibson, I., Rosen, D., & Stucker, B. (2015). Directed Energy Deposition Processes. In I. Gibson, D. Rosen, & B. Stucker (Eds.), *Additive Manufacturing Technologies: 3D Printing, Rapid Prototyping, and Direct Digital Manufacturing* (pp. 245–268). Springer. https://doi.org/10.1007/978-1-4939-2113-3_10

Gurson, A. L. (1977). Continuum Theory of Ductile Rupture by Void Nucleation and Growth: Part I—Yield Criteria and Flow Rules for Porous Ductile Media. *Journal of Engineering Materials and Technology*, *99*(1), 2–15. https://doi.org/10.1115/1.3443401

Khajavi, S. H., Partanen, J., & Holmström, J. (2014). Additive manufacturing in the spare parts supply chain. *Computers in Industry*, *65*(1), 50–63. https://doi.org/10.1016/j.compind.2013.07.008

Koppenhoefer, K. C., Gullerud, A. S., Ruggieri, C., Dodds, R. H., & Healey, B. E. (1994). *WARP3D: Dynamic Nonlinear Analysis of Solids Using a Preconditioned Conjugate Gradient Software Architecture*. https://www.ideals.illinois.edu/handle/2142/14220

Kumar, L. J., & Krishnadas Nair, C. G. (2017). Current Trends of Additive Manufacturing in the Aerospace Industry. In D. I. Wimpenny, P. M. Pandey, & L. J. Kumar (Eds.), *Advances in 3D Printing & Additive Manufacturing Technologies* (pp. 39–54). Springer. https://doi.org/10.1007/978-981-10-0812-2_4

Lambros, J. (2019). *Elastic-Plastic Fracture Mechanics [Lecture]*.

Liu, S., & Shin, Y. C. (2019). Additive manufacturing of Ti6Al4V alloy: A review. *Materials & Design*, *164*, 107552. https://doi.org/10.1016/j.matdes.2018.107552

Najmon, J. C., Raeisi, S., & Tovar, A. (2019). Review of additive manufacturing technologies and applications in the aerospace industry. In *Additive Manufacturing for the Aerospace Industry* (pp. 7–31). Elsevier. https://doi.org/10.1016/B978-0-12-814062-8.00002-9

Pal, R. K., & Geubelle, P. H. (2014). Impact response of elasto-plastic granular and continuum media: A comparative study. *Mechanics of Materials*, *73*, 38–50. https://doi.org/10.1016/j.mechmat.2014.02.006

Panwisawas, C., Perumal, B., Ward, R. M., Turner, N., Turner, R. P., Brooks, J. W., & Basoalto, H. C. (2017). Keyhole formation and thermal fluid flow-induced porosity during laser fusion welding in titanium alloys: Experimental and modelling. *Acta Materialia*, *126*, 251–263. https://doi.org/10.1016/j.actamat.2016.12.062

ParaView. (2021). https://www.paraview.org/

Shunmugavel, M., Polishetty, A., & Littlefair, G. (2015). Microstructure and Mechanical Properties of Wrought and Additive Manufactured Ti-6Al-4V Cylindrical Bars. *Procedia Technology*, *20*, 231–236. https://doi.org/10.1016/j.protcy.2015.07.037

Snow, Z., Nassar, A. R., & Reutzel, E. W. (2020). Invited Review Article: Review of the formation and impact of flaws in powder bed fusion additive manufacturing. *Additive Manufacturing*, *36*, 101457. https://doi.org/10.1016/j.addma.2020.101457

Srivastava, A., Osovski, S., & Needleman, A. (2017). Engineering the crack path by controlling the microstructure. *Journal of the Mechanics and Physics of Solids*, *100*, 1–20. https://doi.org/10.1016/j.jmps.2016.12.006

Srivastava, A., Ponson, L., Osovski, S., Bouchaud, E., Tvergaard, V., & Needleman, A. (2014). Effect of inclusion density on ductile fracture toughness and roughness. *Journal of the Mechanics and Physics of Solids*, *63*, 62–79. https://doi.org/10.1016/j.jmps.2013.10.003

Stone, R. H. V., Cox, T. B., Low, J. R., & Psioda, J. A. (1985). Microstructural aspects of fracture by dimpled rupture. *International Metals Reviews*, *30*(1), 157–180. https://doi.org/10.1179/imtr.1985.30.1.157

Titanium Alloys—Ti6Al4V Grade 5. (2002). AZoM.Com. https://www.azom.com/properties.aspx?ArticleID=1547

Tvergaard, V. (1982). On localization in ductile materials containing spherical voids. *International Journal of Fracture*, *18*(4), 237–252. https://doi.org/10.1007/BF00015686

Tvergaard, V. (1989). Material Failure by Void Growth to Coalescence. In J. W. Hutchinson & T. Y. Wu (Eds.), *Advances in Applied Mechanics* (Vol. 27, pp. 83–151). Elsevier. https://doi.org/10.1016/S0065-2156(08)70195-9

Tvergaard, V., & Hutchinson, J. W. (1994). Effect of T-Stress on mode I crack growth resistance in a ductile solid. *International Journal of Solids and Structures*, *31*(6), 823–833. https://doi.org/10.1016/0020-7683(94)90080-9

Van Hooreweder, B., Moens, D., Boonen, R., Kruth, J.-P., & Sas, P. (2012). Analysis of Fracture Toughness and Crack Propagation of Ti6Al4V Produced by Selective Laser Melting. *Advanced Engineering Materials*, *14*(1–2), 92–97. https://doi.org/10.1002/adem.201100233

VanSickle, R. (2019). *Microscale strain accumulation during fatigue and fracture of additively manufactured Ti-6Al-4V* [MS Thesis]. University of Illinois at Urbana-Champaign.

VanSickle, R., Foehring, D., Chew, H. B., & Lambros, J. (2020). Microstructure effects on fatigue crack growth in additively manufactured Ti–6Al–4V. *Materials Science and Engineering: A*, *795*, 139993. https://doi.org/10.1016/j.msea.2020.139993

WARP3D. (2021). http://www.warp3d.net

Wu, Z., Narra, S. P., & Rollett, A. (2020). Exploring the fabrication limits of thin-wall structures in a laser powder bed fusion process. *The International Journal of Advanced Manufacturing Technology*, *110*(1), 191–207. https://doi.org/10.1007/s00170-020-05827-4

Xia, L, & Shih, C. F. (1995). Ductile crack growth-I. A numerical study using computational cells with microstructurally-based length scales. *Journal of the Mechanics and Physics of Solids*, *43*(2), 233–259. https://doi.org/10.1016/0022-5096(94)00064-C

Xia, Lin, & Shih, C. F. (1996). Ductile crack growth—III. Transition to cleavage fracture incorporating statistics. *Journal of the Mechanics and Physics of Solids*, *44*(4), 603–639. https://doi.org/10.1016/0022-5096(95)00086-0